Development of Radio Science Techniques and a Planetary Mission Concept

by

David Sweeney

A dissertation submitted in partial fulfillment
of the requirements for the degree of
Doctor of Philosophy
(Climate and Space Sciences and Engineering)
in the University of Michigan
2023

Doctoral Committee:

Professor Nilton O. Rennó, Chair
Professor Sushil K. Atreya
Associate Professor James W. Cutler
Assistant Professor Cheng Li

David P. Sweeney

sweendav@umich.edu

ORCID iD: 0000-0003-3334-5227

Dedication

In dedication to my parents, sister Alex, Caitlin and Darby.

Acknowledgements

This research was conducted at both the Jet Propulsion Laboratory, California Institute of Technology and the University of Michigan, under contracts with the National Aeronautics and Space Administration (NASA) mostly through JPL's Strategic University Research Partnerships (SURP) program but in part by the Mars Science Laboratory (MSL) Mission. I would like to thank NASA/JPL and the University of Michigan for the support.

I would like to thank the Science Operations division at JPL for the opportunity to support the MSL environmental observations, furthering our knowledge of Mars.

I would like to thank you my committee members for taking the time to serve on my PhD committee and I for their excellent feedback.

I could not have accomplished this research without my excellent advisor, Nilton Rennó and mentors at JPL, Chi Ao and Panagiotis Vergados. Thank you all for taking the time to mentor me and finding funds for this project. Thank you for all of your help with papers revisions and fantastic suggestions, and for always being available whenever I reached a road block.

Thank you to the CLaSP department for providing an excellent academic environment and rigorous preparation with excellent professors. Thank you to my awesome cohort for the mental support while struggling through coursework together, and for the long nights working on homework in the CSRB.

Thank you to my lab mate Ariana for always supporting my research. Thank you Erik for guiding me over the years. Much of the systems engineering was supported by work from Masters of Engineering students over the past few years, so thank you to everyone involved with the MARiO

team over the years for excellent analysis and supporting our science Goals. Thank you to Remi Free for leading the project and helping me bring everything together into a full mission concept.

Finally, thank you to my family Brian, Jackie and Alex for always supporting me. I could not have done this without all you. And of course, Darby for always being by my side.

Table of Contents

List of Tables

List of Figures

Abstract

Radio Occultation (RO) is a remote sensing observation which takes advantage of radio signals from the communications system of a spacecraft to measure the Doppler shift of the signals as they pass through the atmosphere. Only if the atmospheric composition is known, pressure, temperature and number density can be derived using Abelian transforms. Such observations at Mars are crucial to enhancing modelling software which engineering teams have to use to predict atmospheric conditions during Entry Descent and Landing (EDL), the most high-risk phase of any surface mission.

Most RO experiments at Mars have been performed with an Earth based Deep Space Network (DSN) station and with an orbiting spacecraft at Mars. These observations have to be conducted when the viewing geometry between Earth and Mars is optimal, and they take time away from normal DSN communications tasks for spacecraft operations. As such, the observations lack in the frequency and coverage necessary to properly initialize models used by engineering teams.

RO observations rely on highly precise clocks on board the spacecraft to reduce error in Doppler shift measurements that propagate into the retrieval of physical atmospheric parameters. The Ultra Stable Oscillators (USOs) of these precise clocks are expensive, and require a large volume and power. The use of Commercial off the Shelf (COTS) parts for such a USO is a low-cost solution that provides a less accurate clock. However, we present an analysis that shows the use a Dual One-Way (DOW) frequency method, commonly used in gravity ranging experiments, can achieve the same accuracy as highly stable clocks using a lower stability COTS USO.

Given recent interest in SmallSats for interplanetary missions such as MarCO, a dedicated fleet of SmallSats at Mars is a low-cost solution that could yield unprecedented RO global, diurnal and seasonal coverage. We present a detailed mission concept to use SmallSats over the course of 1 Mars year developed in a collaboration between the University of Michigan and the Jet Propulsion Laboratory (JPL). The concept has been developed in preparation for submission to a NASA SIMPLEx (Small Innovative Missions for Planetary Exploration) call for proposals.

A secondary mission science objective is to measure Electrostatic Discharge (ESD) events, that have been observed during global dust storms (e.g., Ruf et al., 2009; Renno and Ruf, 2012) . Such ESD events present an unknown risk to humans on the surface of Mars. Past Earth based measurements of ESD are lacking in frequency, and the viewing geometry cannot pinpoint the originating source of ESD. However, orbiting spacecraft will have the ability to identify areas which ESD can originate from.

Chapter 1

Introduction

1.1 Mars: Past and Present

1.1.1 Analog to Earth

Mars is the fourth closest planet to the Sun and in many respects is similar to Earth, one important exception is that the Earth generates a protective magnetic field because of its active Iron core while Mars does not. The circulation of the Earth's liquid iron core generates electric and magnetic fields, referred to as a dynamo. Mars had an active core like Earth, but only up to about 100 million years after the planet's formation, convection of the iron core stopped, and the global magnetic field was lost (Roberts et al., 2009). Before Mars lost its dynamo, it is theorized the atmosphere was quite like the Earth's atmosphere with the existence of liquid water that would explain the dry lake beds that rovers on the surface have been exploring. Without an active dynamo, the atmosphere of Mars would have been stripped away by solar radiation because of the planet's low escape velocity, combined with UV ionization and interaction of solar plasma with the upper ionosphere.

Mars is the closest planet to Earth, but its seasons are much longer, being about double the length. A year on Mars is ~687 days, but the length of a day, or sol, is 24 hours and 39 minutes. Gravity on the surface of Mars is also only ~1/3 of Earth's value due to the smaller overall mass of the planet. A full list of basic parameters comparing Mars and Earth are shown in Table 1.1.

Table 1.1 Comparison of basic parameters of Mars and Earth (Williams, 2022).

Bulk Parameter	Mars	Earth
Mass (10^{24} kg)	0.64	5.97
Equatorial Radius (km)	3,396.2	6,378.1
Surface Gravity (m/s^2)	3.71	9.80
Escape Velocity (km/s)	5.03	11.19
Sidereal Orbit Period (days)	686.98	365.26
Semimajor Axis (AU)	1.5	1

1.1.2 The Atmosphere of Mars

The thin atmosphere of Mars has been slowly stripped away by the interaction between the upper atmosphere and the solar wind. The resulting pressure at the surface is a fraction of Earth at an average of 600 Pa. The composition is mostly CO_2 with N_2 and Ar as secondary contributors and trace amounts of O_2 as referenced in Table 1.2.

Table 1.2 Mars atmosphere is mostly composed of CO_2, N_2, Ar, and O_2 with other trace gasses (Trainer et al., 2019*)*.

Gas	Mean % of Atmosphere
CO_2	95.1
N_2	2.6
Ar	1.94
O_2	0.161

Water in the liquid state is not stable while exposed to the atmosphere due to the extremely low surface pressure and temperature, it will freeze almost instantaneously. Trace amounts of water can be detected in the atmosphere as vertically integrated precipitable (pr) amounts of the order of 5 to 100 $pr \cdot \mu m$ depending on the season (Carr, 1987). This is many orders of magnitude lower than on Earth that has ~1,000 $pr \cdot cm$. Water can mostly be found frozen below the surface of Mars, and at the Northern pole during the summer when the CO_2 caps evaporate exposing the water ice underneath (Carr, 1987).

1.1.3 Global and Regional Dust Storms

Global dust storms on Mars play a crucial role in the weather dynamics. During a dust storm, large amounts of dust are transported high into the atmosphere which insulate the lower portion of the atmosphere, and heat up the upper atmosphere by absorbing solar radiation (Streeter et al., 2020). These storms typically occur in the summer months of the southern hemisphere on Mars, and Global Dust Storms typically occur once every two Earth years.

To illustrate how the vertical temperature profiles change, we analyzed data from the Mars Climate Sounder (MCS) instrument on board Mars Reconnaissance Orbiter (MRO). The infrared and visible spectrometer measures temperature, pressure, water vapor and dust. However, due to the average dust size of 1.5 μm, the infrared channels of MCS are highly sensitive to dust and cannot penetrate all the way to the surface during intense dust storms as shown in Figures 1.1 and 1.2. A more uniform temperature profile is illustrated across all

latitudes in Figure 1.1, and MCS measures the temperature from the top of the atmosphere down to the surface, while in Figure 1.2 the signal does not reach the lower atmosphere.

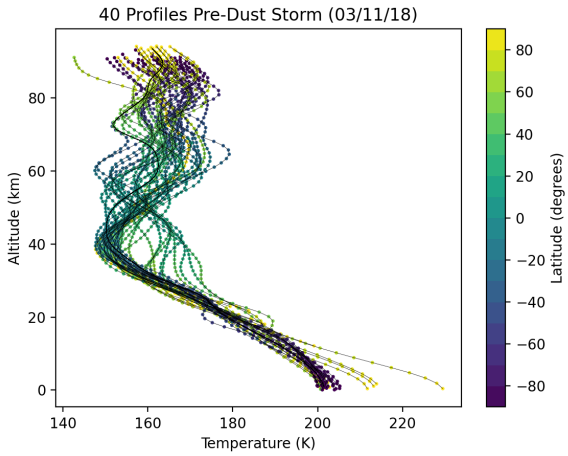

Figure 1.1 MCS profiles at 0º longitude and all latitudes at clear conditions just before the 2018 global dust storm. Uniform temperatures can be seen at all latitudes extending to the surface.

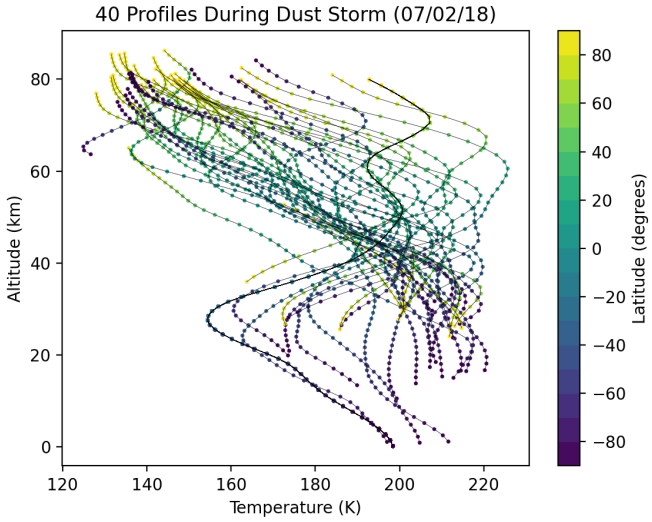

Figure 1.2 MCS profiles at 0º longitude and all latitudes during the beginning phase of the 2018 global dust storm. Overall the temperatures increase, especially in the upper atmosphere where the dust absorbs UV radiation strongly.

Regional dust storms are quite different from global dust storms in a number of distinct aspects (Kass et al., 2020). Global storms have only been observed in the summer months of the southern hemisphere, where regional storms can occur in all seasons. Global storms also last

much longer and transport dust to higher altitudes than regional storms. Absolute peak daytime temperatures during global storms exceeds 235 K while in regional storms they are smaller than 225 K. However, the sample size for differentiating between the two types of storms are small with 3 global events and around 20 large scale regional dust storms cataloged.

1.2 Remote Sensing: Justification for this Work

1.2.1 Detecting Electrostatic Discharge Events

Dust storms, specifically global dust storms, transport large amounts of dust high into the atmosphere. Saltation and dust lifting causes charging which generates electromagnetic fields. As the lighter, negatively charged, dust particles are transported higher in the atmosphere, a large electric field can be generated from the charge separation with larger positively charged particles near the surface and smaller, negatively charged particles, aloft (Harrison et al., 2016; Rennó et al., 2003; Rennó & Kok, 2007). The negatively charged particles are typically smaller in size and can be picked up by winds much easier than saltating particles.

Large electric potentials are a product of the charge separation during dust storms. Electric discharges have been detected during such storms using innovative spectrometer detectors that are sensitive to non-thermal radiation by measuring higher order moments of electric field strength (Ruf et al., 2009). This process uses a Kurtosis estimator to detect such events, it is a statistical tool that measures the “tailedness” of a distribution. However, such events have yet to be detected again, but a project with JPL uses the same type of spectrometer deployed on a DSN station in Madrid to passively analyze Mars based communications signals. These electrostatic discharges (ESD) present an unknown risk to surface assets and future human exploration. Such detectors can be miniaturized and take advantage of the emitted communications signals at Mars to passively measure the strength of these ESD events.

1.2.2 A History of Radio Occultation

Radio Occultation (RO) is a remote sensing technique first used at Mars on Mariner 4 in 1965 by an experiment that yielded results on the neutral atmosphere refractivity and density as well as electron density of the ionosphere (Kliore et al., 1965). A full description of RO can be found in Chapter 2.1. RO has been implemented on most planetary missions and only requires a communications system and a stable clock. Traditionally, these observations are accomplished using the orbiting spacecraft and Deep Space Network (DSN) back on Earth. As a result of scheduling over the DSN and correct viewing geometry with the spacecraft at Mars, the number of RO observations are limited. For example, MRO has a less stable clock on board, so a two-way RO experiment is ideal for higher accuracy measurements. This means that the highly stable clock on the DSN ground station transmits, is received by the spacecraft, then transmitted back to Earth. Even though these measurements are more ideal, they can only be accomplished as the spacecraft enters the limb from the perspective of the DSN station. Figure 1.3 from (Hinson et al., 2014) shows the distribution of RO experiments over the course of 3 Mars years. Panel a illustrates the spatial distribution is limited to certain latitudes over seasonal variations, and panel b illustrates that observations are extremely limited over the diurnal cycle. The two-way observations are shown as orange dots and the black are less accurate one-way observations.

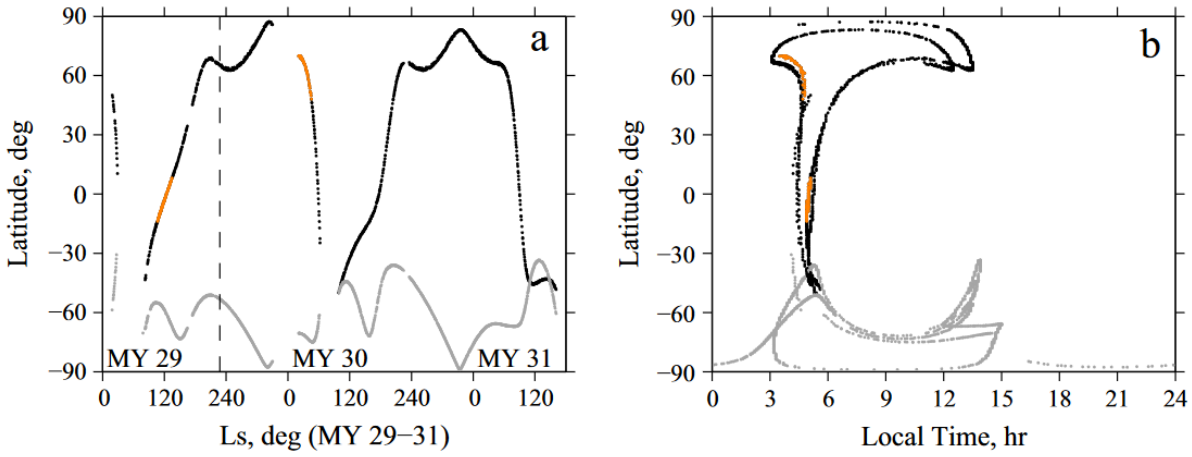

Figure 1.3 Coverage of MRO RO observations from January 2008 (L_s = 18º of MY 29) through August 2012 (Ls = 161º of MY 31). Black and gray dots denote measurements at occultation entry and exit, respectively, whereas the two subsets of entry-side measurements discussed in this paper are shown in orange. The dashed vertical line denotes the start of coordinated observations by the MCS. From (Hinson et al., 2014).

1.2.3 Use of SmallSats for Interplanetary Exploration

The use of SmallSats, particularly for planetary exploration has gained traction in recent years. The first successful use of SmallSats at Mars was accomplished with the Mars Cube One (MarCO) mission that acted as a data relay for the InSight landing in 2018 (Schoolcraft et al., 2016). Relay operations were a success with the use of a high gain, deployable reflector array antenna that transmitted radio signals directly to the DSN back to Earth.

A dedicated mission of SmallSats for cross-link RO observations would be a low-cost solution to yield unprecedented diurnal and seasonal coverage of Mars at all latitudes. Instead of ~1 RO observation a day, a fleet of SmallSats could accomplish 50-100 full vertical profiles per day (Moeller et al., 2020; Sweeney et al., 2021). SmallSat missions usually require a much smaller budget and have volume and power constraints. A smaller clock must be implemented to realistically fit inside a 6U SmallSat. However, in chapter 3, we introduce a novel dual one-way

(DOW) concept used in gravity ranging experiments (Thomas, 1999) that can achieve the same accuracy as traditional RO experiments on larger spacecraft.

1.2.4 Supporting Entry Descent and Landing (EDL)

A dedicated SmallSat mission could close an existing knowledge gap that exists for engineering teams that use global and mesoscale models to plan for extreme conditions during the EDL phase (Kass et al., 2003), which is the most dangerous portion of any surface mission. Currently, the mesoscale models used for generating landing site conditions are initialized by global scale models. If enough real data existed for RO profiles globally, the data would be used to accurately initialize the mesoscale models for more accurate EDL predictions.

Requirements for landing humans on the surface of Mars are expected to be stricter than landing autonomous spacecraft. The Mars Exploration Analysis Group (MEPAG) are tasked with identifying the top science objectives for Mars for the next proposed Mars missions. A specific science goal (IV) from (Banfield, 2020) pertains to prepare for human exploration. Addressing this goal is achieved through characterizing atmospheric factors via RO profiles to inform future EDL efforts.

Chapter 2

Enabling Mars Radio Occultation by SmallSats

This chapter has been published as a journal article reproduced below: Sweeney, D., Ao, C., Vergados, P., Rennó, N., Kass, D., & Martínez, G. (2021). Enabling Mars Radio Occultation by SmallSats. *2021 IEEE Aerospace Conference (50100)*, 1–12. https://doi.org/10.1109/AERO50100.2021.9438147

Abstract

We introduce a Mars Radio Occultation (RO) mission concept leveraging on small satellite (SmallSat) technologies that will enable measurements that address both Mars science and exploration priorities. The RO technique measures the Doppler shift of radio signals of a spacecraft occulting behind a planet's limb, providing information about the planet's atmospheric density, temperature, and pressure profiles. We design a SmallSat constellation and simulate "crosslink" RO observations between the SmallSats to determine the expected accuracy and spatiotemporal coverage of Mars RO atmospheric profiles. Such measurements are key to spacecraft Entry, Descent and Landing (EDL), and Ascent from the Surface (AST) of Mars. Today, the number of Mars atmospheric profiles measurements with high vertical resolution is

limited, especially near the surface where satellite based passive measurements are inhibited by atmospheric absorption. We find that crosslink ROs between a constellation of six SmallSats provide global and diurnal cycle coverage with dozens of occultations per day, providing temperature information from near-surface up to ~45 km with altitude dependent accuracy that ranges between <0.5 K at lower altitude to <5 K in the middle-to-upper atmosphere. Ionospheric ROs measure the electron density with accuracy of ~5 – 10% at the peak ionospheric height between 100 and 140 km. We conclude that measurement by a SmallSat constellation can augment existing observing platforms by reducing observational gaps and yield high resolution measurements required for safe spacecraft operations during EDL and AST.

2.1 Introduction

RO is a limb sounding technique that yield vertical profiles of the refractivity of a planet's atmosphere via precise measurements of Doppler shifts as radio signals pass through the atmosphere (Hajj et al., 2002; Hinson et al., 1999; Vogt et al., 2016) (Figure 1). RO has been successfully used in interplanetary missions starting with Mariner 4's flyby of Mars in 1965 (Kliore et al., 1965; Vogt et al., 2016). Traditionally, RO experiments were performed using radio links between a spacecraft and an Earth-based Deep Space Network (DSN) antenna (Hajj et al., 2002; Vogt et al., 2016; Withers, 2010). Constraints in the observing geometry limit the number of measurements and their spatiotemporal distribution. Many knowledge gaps in the climate of Mars have been identified by the science community (Table 2.1), and given recent interest in human missions to the planet, it is imperative to begin increasing observational data to improve existing climatological models and to give operations teams accurate data to safely land spacecraft on the surface.

The mission concept we propose utilizes a dedicated fleet of SmallSats to make global, high temporal RO measurements from the surface to the top of Mars' atmosphere. By removing the Doppler shift due to the relative motion of the spacecraft, the "excess" Doppler shift introduced by the planet's atmosphere is estimated. With knowledge of the spacecraft position and velocity vectors, the excess Doppler shift is converted into a bending angle as function of the impact parameter (defined as the closest distance of the radio wave ray path from the planet's limb). The planet's atmospheric refractive index is then estimated by the bending angle, using either the ray tracing or the Abel transform technique (Born et al., 1980). Knowing the chemical composition of the planet, the atmospheric refractivity provides information about the neutral air density, pressure, and temperature, as well as the total electron content (TEC) of the ionized portion of the planet's atmosphere. The relative motion between the spacecraft and the Earth's DSN antennas has allowed measurements of bending by the rings of Saturn (Marouf & Tyler, 1982), the atmosphere of the Earth (Ware et al., 1996), and the atmosphere of Mars (Ao et al., 2015; Hinson et al., 1999, 2014; Oudrhiri et al., 2020). The accuracy and resolution of these measurements are determined by the orbital configurations of the spacecraft, and the precision of their on-board clocks. Our goal is to determine the instrument requirements necessary to meet a set of engineering requirements derived from the goals of the Mars Exploration Program Analytics Group (MEPAG) for future human exploration and a set of science requirements derived from the goals of the Decadal Survey Report.

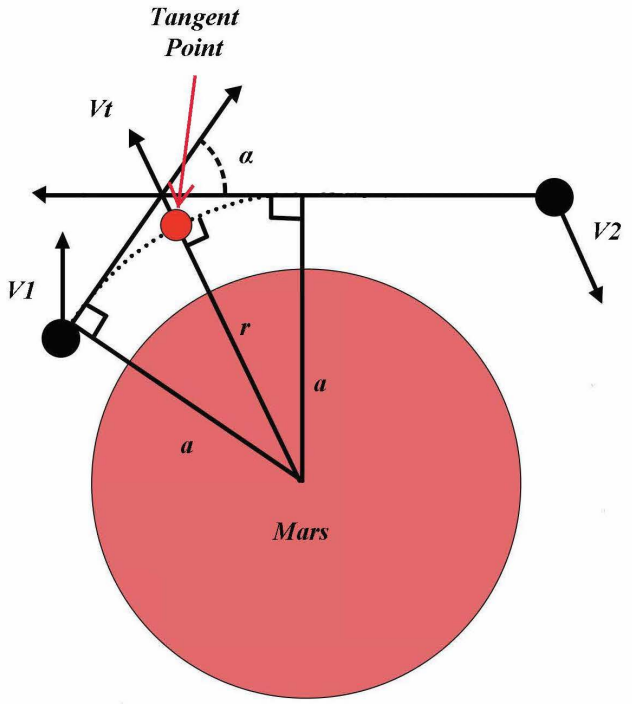

Figure 2.1 Spacecraft RO geometry (Adapted from (Hinson et al., 2014; Withers, 2010)). The dashed line represents the radio wave ray bending due to the presence of the Martian atmosphere. The tangent point velocity (Vt) and sampling rate affect the accuracy of vertical atmospheric profile me measurements. Figure illustrates radius of tangent point (r), impact parameter (a), bending angle (α), velocity vector of spacecraft 1 (V_1) and velocity vector of spacecraft 2 (V_2).

2.2 Motivation

2.2.1 Background

The most dangerous phase of any landed martian mission is EDL, where fast-varying atmospheric conditions that could lead to a mission failure are encountered. JPL currently utilizes martian atmospheric mesoscale models, initialized with data from a Mars Global Circulation Model (GCM), to plan EDLs. In addition, to surface pressure data obtained from traditional RO, the Viking Landers, InSight, and the Mars Science Lab (MSL). Temperature profiles (used to calculate density profiles) are provided by Mars Climate Sounder (MCS) (McCleese et al., 2007), and the Thermal Emission Spectrometer (TES) (Christensen et al., 2001). MCS and surface pressure data are merged with the mesoscale model results, and high

frequency perturbations, to produce optimized predictions for engineering purposes (M. P. Golombek et al., 2003; Kass et al., 2003; Tamppari et al., n.d.). Dust conditions in the atmosphere are a key driver of the meteorology due to the fast response of the thin martian atmosphere to changes in airborne dust. Thus, mesoscale models are often run over a variety of possible (and less likely, extreme) dust scenarios (M. Golombek et al., 2017, 2020). For successful engineering efforts, it is important that both the mean (or climate) and the extrema (or weather) be well represented in the models. The former provide the most likely case for design while the latter provide the range of conditions that the landing system needs to survive.

Several limitations in the current observations restrict the ability of EDL performance to be optimized (and thus deliver more mass to the surface with less risk) that can be mitigated by RO from a constellation of SmallSats. The RO technique has much better vertical resolution than that of most current datasets (~1 km versus 5 km to 10 km). In addition, RO is particularly sensitive to the temperature in the lowest ~20 km where it is of most interest and where thermal infrared (IR) techniques have difficulties due to aerosols. The primary atmospheric datasets (TES and MCS) are limited in local time coverage while RO from a constellation can access all local times (while there are datasets with local time coverage e.g. from the Trace Gas Orbiter, they often suffer from not sampling all local times simultaneously). Considering the recent use and interest of SmallSats for RO experiments at Mars, such as MarCO (Oudrhiri et al., 2020) and MOSAIC (R. J. Lillis et al., 2020), this mission concept leverages on similar technologies.

While RO does not directly measure surface pressure, the temperature profiles extend sufficiently close to allow for a very accurate estimate (Withers, 2012). Note that while RO between an orbiter and the DSN has some of these advantages, the coverage and number of profiles are extremely limited in comparison those obtained by an orbiting constellation.

Motivated by these needs, we developed the conceptual design for a SmallSat RO constellation mission and developed a simulation code to augment existing Mars atmospheric profiles. We also performed sensitivity experiments to quantify the impact of different noise sources on the retrieved RO profiles and determine the acceptable noise level that meets the mission requirements in MEPAG. The mission concept we propose is capable of filling significant gaps thus constraining Mars atmospheric models and increasing the information available for EDL. The specific mission concept requirements depend on the mission type targeted. Aerobreaking, aerocapture EDL, and ascent from the surface (AST) present unique challenges because they require varying degrees of atmospheric measurement accuracy.

Table 2.1 A preliminary science traceability matrix responding to the Decadal Survey Report goal of achieving science with CubeSats – Thinking Inside the Box, Goal IV of MEPAG 2020 survey 'Prepare for human exploration'.

Recommen-dations	Project Objectives	Science and Engineering Requirements		Instrument Requirements		Projected Perfor-mance	Mission Requirements
		Observable Parameter	Physical Parameter	Accuracy & Precision	Sampling rate		
Understand the processes that control the variability of the present-day climate	**Objective 1**: Mature the concept for measuring the neutral density profile from near the surface to the	Refractivity profile of the neutral atmosphere with accuracy of 1% and vertical resolution of 1 km (< Planetary Boundary Layer depth)	Doppler frequency measurements Doppler measurements at two radio frequencies (bands at 0.4, 2,	$\sigma\Delta f/f \approx 4 \times 10^{-13}$	~10 Hz	$\sigma\Delta f/f \sim 10^{-13}$	Meas-urements for at least one Martian year

Recommen-dations	Project Objectives	Science and Engineering Requirements		Instrument Requirements		Projected Perfor-mance	Mission Requirements
		Observable Parameter	Physical Parameter	Accuracy & Precision	Sampling rate		
Conduct atmospheric measurements and develop models for evaluation of aerocapture (P-SAG)	upper atmosphere **Objective 2**: Mature the concept for measuring the electron density profile of the ionosphere and its variability	Differentiate the effects of neutral constituents from those of free electrons Temperature accuracy within 1 K and vertical resolution of 0.5 km between 6-12 km for parachute deployment	8 & 32 GHz are being considered)				Measure-ments over the entire local diurnal cycles and across the globe A constellation of SmallSats
		Refractivity profile of the ionosphere with accuracy of 5% and vertical resolution of 5 km (~ ½ scale height)	Doppler frequency measurements	$\sigma\Delta f/f \approx 10^{8}/f^{2} \approx 10^{-13}$ (at 2, 8 & 32 GHz)	~10 Hz	$\sigma\Delta f/f \sim 10^{-13}$	
		Refractivity profiles with global coverage throughout diurnal and seasonal cycles (1 Martian year)	As above	As above	~100 global profiles per day	Depends on the number of satellites and their orbits	

2.2.2 MEPAG Goals

The driving requirements of the mission concept we propose are derived from MEPAG, Goal IV, 'prepare for human exploration' (Banfield, 2020). These science requirements are listed in the science traceability matrix (Table 1).

The top mission science and engineering goals were derived from 2020 MEPAG goals and input from JPL scientists and engineers that participated into the Mars Science Laboratory (MSL), Phoenix and InSight missions. The latter input is presented in the following section as considerations instead of hard requirements, which allow for flexibility in the mission trades and design. With the current RO capabilities, these considerations are discussed, and the most stringent are listed as requirements in Table 2.1. The engineering goals are mission-dependent (robotic or human) and whether or not the mission uses ballistic or guided entry.

The knowledge of the thermal state of the martian atmosphere up to 80 km is key to designing orbital capture and EDL for human scale missions to Mars, and to improving predictive capabilities of numerical models through validation (Smith et al., 2004). Furthermore, knowledge of temperature profiles within Mars Planetary Boundary Layer ($\lesssim$10 km) is important because such profiles inform of the convective and turbulent behavior of the temperature perturbations, which govern the transfer of heat, momentum, and molecular species at the surface-atmosphere interface (Smith et al., 2004). MEPAG Goal IV, Investigation A1.1 calls out measurements of the global temperature field from the surface to ~80 km with a 5 km resolution at all local times. Investigation B3.3 focuses on temperature profiles within dust storms in the lowest 20 km (80 km in a global dust storm) with a vertical resolution < 5 km, emphasizing the importance of observations through aerosols. Finally, Investigation B3.2 calls for surface pressure and near surface meteorology over various temporal scales. The MEPAG Goals

document considers all three of these as high priority to fill in current gaps necessary to land humans on Mars.

Radio occultation observations from a constellation of SmallSats in Mars orbit are expected to be able to make significant progress on the investigations recommended by MEPAG. We focus on designing and optimizing a mission concept and analyzing its coverage (spatial and local time) as well as studying the necessary tradeoff in occultation performance and noise to achieve the listed requirements.

2.3 Methodology

RO experiments rely on highly precise timing to capture the small delay in the signal that is caused by atmospheric bending. Small sources of uncertainty of the spacecraft location and time measurements must be considered and characterized. In order to assess the spatial and temporal coverages from the SmallSat constellation and to accurately map the measurement uncertainty to the retrieval uncertainty, we have developed an end-to-end process (see Figure 2.2) by first building a satellite constellation in order to maximize the number of RO opportunities per day using the Systems Toolkit Software (STK). The velocities based on the geometry of the spacecraft are fed into a Python code which determines the Doppler shift, then artificial noise is added to replicate uncertainties in this shift as it relates to velocity and position errors. These uncertainties are directly related to pressure, temperature, neutral and electron number density.

In this study, we utilize a synthetic or observed (e.g., from actual Mars Global Surveyor (MGS) RO retrieval) refractivity profile to use as basis for our sensitivity analysis. Specifically, we will account for instrument error by varying the levels of thermal and phase noise on the reference profile. We characterize the RO retrieval errors through comparison of the results of

the RO simulations obtained using the bending angle measurements with noise added with the original MGS and synthetic profiles. Through the use of a dual frequency band radio, data on the state of both the neutral atmosphere and ionosphere is obtained.

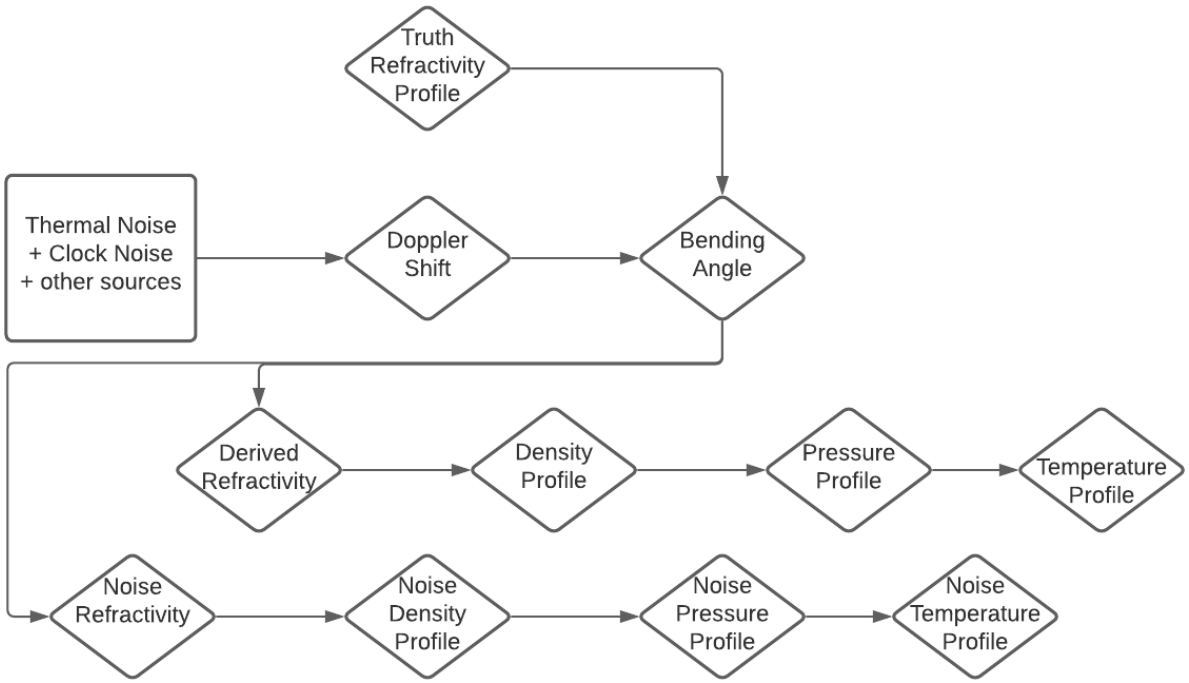

Figure 2.2 This flowchart illustrates how simulation code converts Doppler shift to temperature, and how noise propagates into retrieval uncertainty.

2.4 Results

To determine the coverage and resolution of the measurements simulated, the STK is used to simulate and optimize orbital configurations. Given a set of orbital parameters for the spacecraft in the constellation, the line-of sight between each pair of spacecraft is computed to determine occultation opportunities. An occultation opportunity is defined as one where the ray tangent point altitude varies continuously from -20 km to 200 km (egress) or vice versa (ingress) to successfully measure the ionosphere and neutral atmosphere. For each occultation, the

location and vertical velocity of the tangent points are computed at each altitude step (with a sampling rate of ~1 Hz). Inertial positions of each spacecraft are used to determine the geometry and calculate the velocity of the tangent point (Figure 2.1) as determined by (Hajj et al., 2002). The capability to simulate RO spatial and local time coverages over an extended period using STK would allow us to experiment efficiently with different constellation configurations as we move forward with the mission design. We consider several orbital configurations as part of an ongoing trade study. In each of the configurations mentioned, all employ co-rotating (same direction) orbits since they are more easily realized in a single launch. Additionally, high inclination orbits are simulated in each of the following configurations to maximize coverage at all latitudes. By combining the motion of the spacecraft with the revolution of the planet, it allows for the precession that leads to easily achievable global coverage. The different orbit altitudes of the spacecraft allow for the vertical profiles of the atmosphere to be determined

2.4.1 Configuration 1

Figure 2.3 shows a constellation consisting of 6 SmallSats with 4 outer polar-orbiting satellites in two orbital planes at an altitude of 7,000 km. The 2 satellites acting as receivers have an inner orbit altitude of 250 km and 70° of inclination. This configuration provides global coverage with around 200 RO opportunities per day. However, this configuration was found to be expensive in terms of delta-V for insertion (12.63 km/s).

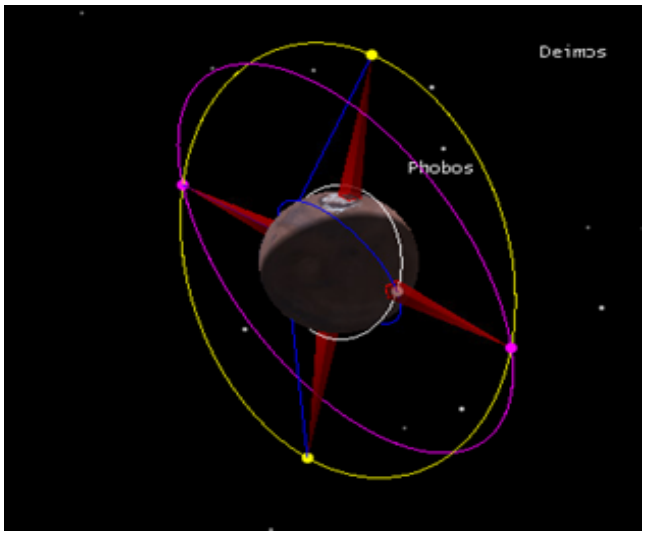

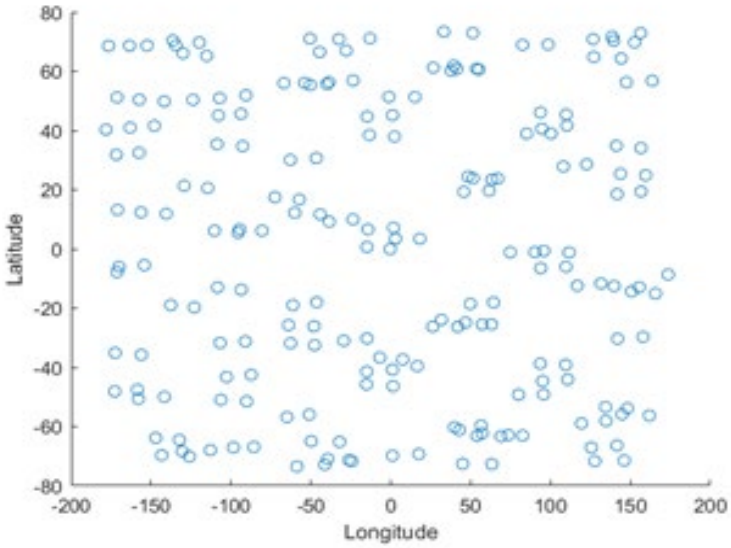

Figure 2.3 Example of orbital configuration with 4 outer polar orbiting spacecraft in 2 planes. 2 inner spacecraft, 2 orbital planes.

2.4.2 Configuration 2

A similar constellation was achieved by simplifying the orbital configuration in Figure 2.3. Figure 2.4 shows a constellation with similar coverage, but only requires an insertion delta-V of 1.88 km/s. However, the number of profiles per day average around 160 as opposed to 200, but still meet the requirements of ~100. The average duration of a full atmosphere occultation was 330 s, the shortest was 327 s and the longest spanned 336 s.

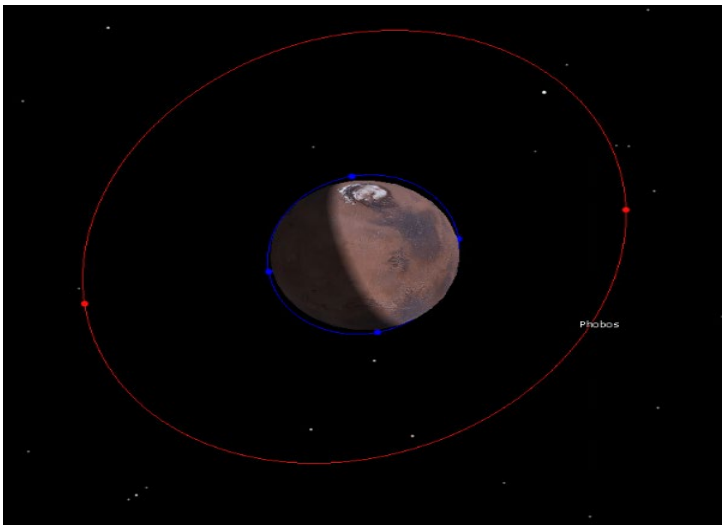

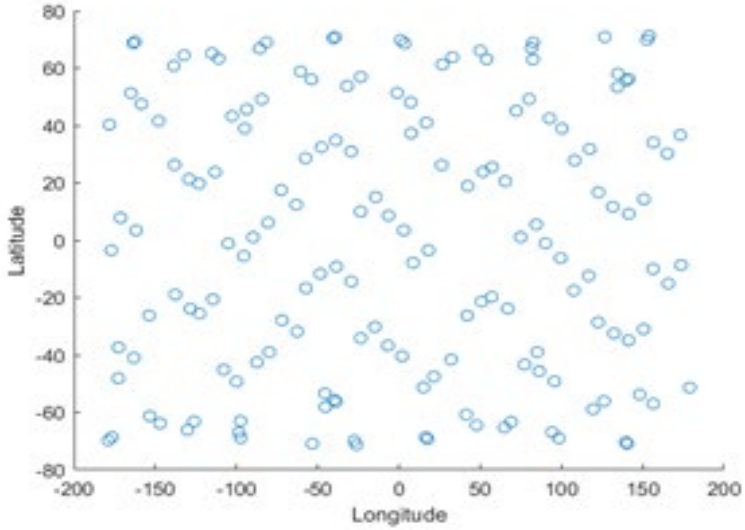

Figure 2.4 Simplified orbital configuration with 2 outer spacecraft in 1 orbital plane at 80° inclination, 4 inner spacecraft in 1 orbital plane at 70° inclination.

2.4.3 Configuration 3

A third configuration that deploys all spacecraft in the same orbital plane at different altitudes with and inclination of 90° was considered. Specifically, 2 at 330 km, 1 at 706 km, 1 at 1350 km and 2 at 3095 km. The differing orbit radii will lead to a nodal precession, which causes the longitudes covered to spread out over time. This configuration in particular was difficult to

implement to meet our goals since the coverage over the time of the mission is always subject to change. This deployment requires similar delta-V to Figure 2.4. Statistics were gathered at different points in the mission for 1 Martian year. At 0, 3 and 6 months there are 118 RO tracks per day. Starting at 12 months, 229 tracks and finally 24 months with 363 tracks. Spacecraft plane separation can be seen in Figure 2.5 over the course of 1 Martian year.

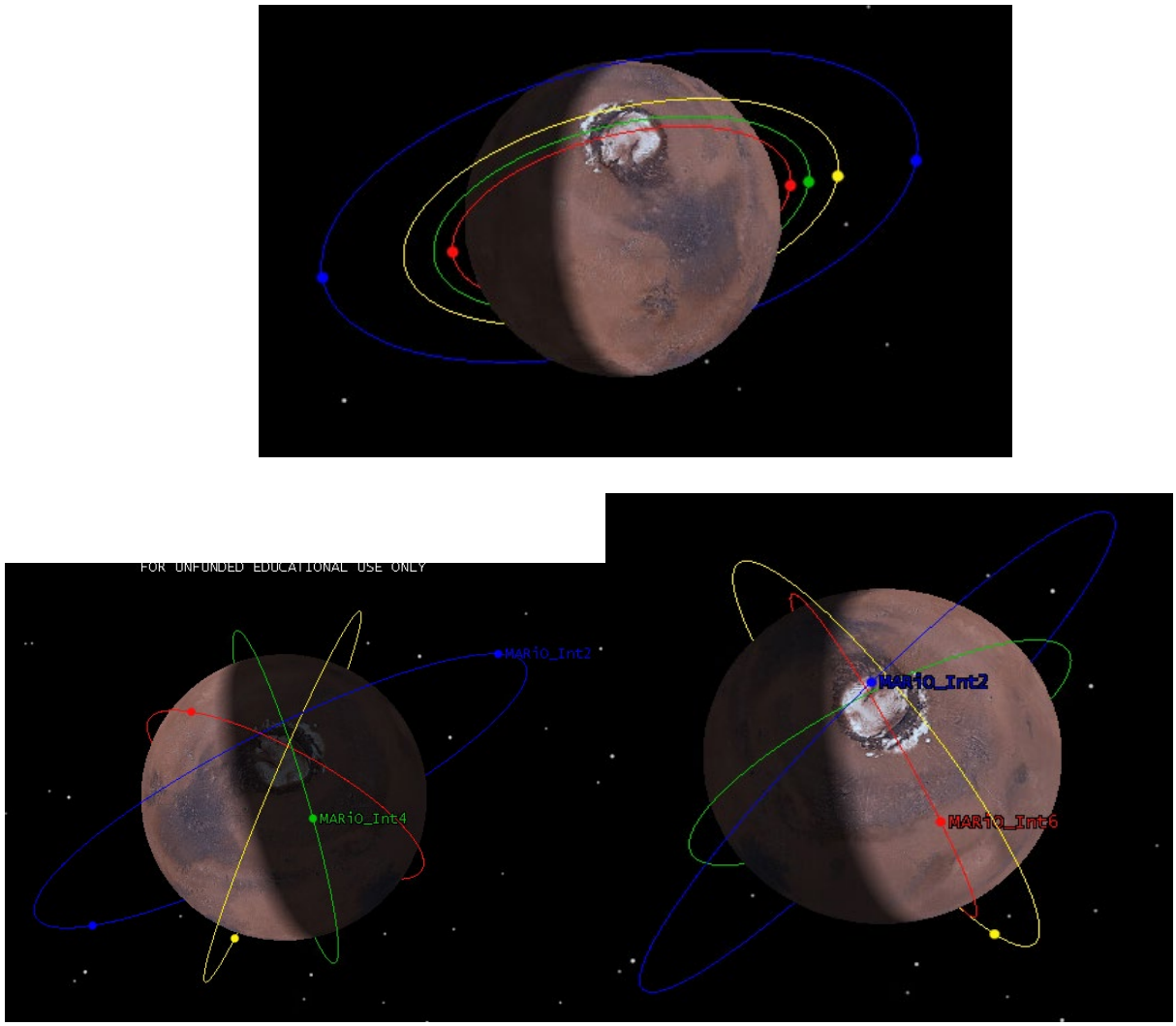

Figure 2.5 Initial deployment of spacecraft at different altitudes (top) and separation due to nodal precession at 0 (top), 12 (middle) and 24 (bottom) months.

The current optimal orbital configuration (Configuration 2) has relatively low tangent point velocity. Vertical profiles between a transmitting and receiving spacecraft span from 200 km above the surface to -20 km (in order to account for the Doppler delay of the signal). Considering 1 Hz sampling, the vertical resolution varies from ~0.4 km at 200 km to ~0.9 km at the surface. To meet the 0.5 km resolution requirement at the surface, the orbital configuration would need to be modified to reduce the relative velocity of the spacecraft or, to reduce the sampling rate to 0.50 Hz. However, all configurations studied so far meets the main requirement in Table 2.1 of ~100 profiles per day. The final mission architecture and orbital configurations will be selected based on the budget available for the mission.

2.4.4 Retrieval Simulation

We have developed a set of Python programs that propagate Doppler shift, or bending angle, uncertainty to refractivity and subsequently to density, temperature, and pressure. RO instrument performance can be specified in terms of the Doppler shift error. The Doppler residual (where the Doppler shift due to orbital motion and other non-atmosphere effects are removed) can then be used to compute a vertical profile of ray bending angles. The uncertainty in bending angle is directly proportional to the Doppler shift uncertainty (Hajj et al., 2002). We note that the Doppler shift error depends on integration time (assumed to be 1 s here unless indicated otherwise), which relates to the vertical resolution through the velocity of the tangent point altitude. For example, for tangent point velocity of 1 km/s, the vertical resolution is 1 km for a 1 s integration time. The vertical resolution can be improved by reducing the relative spacecraft velocities through carful choice of the orbital configurations.

The dominant contributions to the Doppler or bending angle uncertainty are expected to be from thermal noise and clock instability. For simplicity, we assume each of these noise

contributions to be uncorrelated and model them as white noise, as laid out in the following section. Given a total noise level of sigma for the bending angle, we can generate different realizations of bending angle noise and derive the retrieval uncertainty statistically via the Monte Carlo method. We start the simulations with a "true" bending angle produced either by empirical data or artificially created. Then we compute the retrieved refractivity and corresponding physical quantities. For each realization of random noise, the random noise is added to the "true" bending angle, which is used to retrieve the noisy refractivity and other parameters. The difference represents the retrieval uncertainty for each parameter. Repeating this for many realizations (100), we can compute the root-mean-square error for each parameter as illustrated in Figure 2.2. The total bending angle noise added to each profile determined previously depends on clock stability, integration time, transmitter/receiver, antenna and selected frequency. We consider 3 different Allan Deviations (AD) over 1s time intervals. 1×10^{-12}, 1×10^{-13} based on Mars Global Surveyor clock specifications given by (Hinson et al., 1999), and 4×10^{-13} of the requirements in Table 2.1. The expected bending angle uncertainties determined using equations A1-A5 are then found to be 0.3, 0.03 and 0.12 μrad.

2.4.5 Thermal Noise

Generally, if a highly precise USO is specified, the source of most of the noise is derived from the electronics onboard the spacecraft. The thermal noise is directly related to the signal-to-noise ratio (SNR) which in turn relies on the orbital configurations as well as the transmitter and receiver antennas and RF electronics. The uncertainty in thermal noise is based on equation A6 (Withers, 2010). The thermal noise is estimated using equation A6, and converting the Doppler shift uncertainty to a bending angle uncertainty using equation A5. For 1 Hz measurements, the time interval is 1 s and a typical value for the noise bandwidth is 100 Hz (Hinson et al., 1998;

Withers, 2010). The SNR for a typical antenna gain of 5 dBi and transmitter power of 5 W (typical for SmallSats) yields ~67 dB for UHF and ~41 dB for X-band. The resulting uncertainties for thermal noise can be calculated as ~1 mHz for UHF and ~20 mHz for X-band.

2.4.6 Clock Noise

The radio occultation technique is essentially a timing measurement of the slight delay in the radio signal as it traverses the atmosphere and ionosphere of the target planet. As such, it is important for both the transmitter and the receiver to carry a clock or oscillator that is stable over the timescale of a RO observation (~1-100 s). The stability of an oscillator is often characterized by its Allan deviation (AD) given in units of s/s over different time intervals. Oscillator noise is time-scale dependent and therefore can be better described in terms of its phase power spectrum. However, here we adopt a simple approach aimed at providing a first-order characterization on the effect of clock noise by modeling it as white noise (equations A1-A5). Finally, the total expected noise can be calculated as the root-square-sum of the phase and thermal uncertainties since they are treated as uncorrelated Gaussian distributions (equation 1). The final uncertainty values for each AD and frequency are summarized in Table 2.2.

$$\sigma_{total} = \sqrt{\sigma_{thermal}^2 + \sigma_{clock}^2} \quad (1)$$

Table 2.2 Total thermal and phase uncertainties converted to bending angle uncertainties for different Allan Deviations.

Allan Deviation	X-Band Total Bending Angle Uncertainty (μrad)	UHF Total Bending Angle Uncertainty (μrad)
1.00E-12	0.376	0.402
1.00E-13	0.229	0.269
4.00E-13	0.256	0.293

2.4.7 Neutral Atmosphere Simulations

The simulations presented in this paper employ a synthetic exponential refractivity profile that is initialized at the surface with the expected value of 3.82 N-units (Ao et al., 2015) as a function of altitude. Alternatively, the program is able to import MGS data consisting of pressure, temperature, number density and radius of each measurement. The pressure and temperature are converted to a refractivity using the relationship from (Ao et al., 2015; Ho et al., 2002).

$$N = 1.306\frac{P}{T} - 40.3 \times 10^6 \frac{n_e}{f^2} \quad (2)$$

Where pressure is in Pa and temperature is in degrees K. The constant in front of $\frac{P}{T}$ is a direct empirical relationship of the air refractive index to the pressure and temperature of the dry atmosphere, with the unique gas composition of Mars' atmosphere. The constant in front of the second term is a conversion factor between the refractive index (n) and the refractivity (N) as it

depends on the frequency of the transmitted signal and the electron number density. Refraction has a direct relation ship to these physical parameters, and therefore is the important parameter we must determine from crosslink Radio Occultation observations. When determining the refraction, we must consider scattering, absorption and multipath of the signal in the atmosphere. At Mars, the atmosphere is thin enough that the absorption of the signal is negligible and we only measure the phase of the received signal. However, depending on the transmitted frequency, sand or dust particles can cause attenuation or scattering of the signal if the particles are on the same order of magnitude as the wavelength. Multipath propagation occurs when radio signals are refracted or reflected of surfaces near the antenna and have a direct relationship to the surface are of the spacecraft. Since we are considering SmallSats, multipath is also negligible since the surface area is small. In order to retrieve a meaningful vertical profile of the atmosphere, we depend on an initial reading of either temperature or pressure near the surface or at a high altitude to initialize the expected vertical profiles. We therefore rely on readings from rovers at the surface or external orbiting spacecraft instruments such as Mars Climate Sounder (MCS).

Since we are considering the neutral atmosphere, we ignore the second term that gives the electron density and note that it is frequency dependent. Synthetic RO profiles at X-band were created that include a total noise level (thermal and phase) that corresponds to the ADs in Table 2.2. The RMSE is calculated from the derived noiseless, and the noise added profiles from the surface up to ~40 km. All USOs considered meet the surface pressure requirement of 3 Pa at the surface (Figure 2.6, bottom left panel). However, the final temperature RMSE values at the surface (Figure 2.6, bottom right panel) reveal that only the USOs with $1x10^{-13}$ and $4x10^{-13}$ AD will meet the surface requirement of ~1 K (vertical black line) temperature accuracy between 6 and 12 km (horizontal red lines). These AD also meet the projected performance of Objective 1

in Table 2.1 (~$1x10^{-13}$). Sources of uncertainty in these simulations mainly stem from the thermal noise (communications system and electronics on board) and clock noise (from the USO itself). However, other sources of uncertainty can come from the initialization of the expected profiles themselves and error due to the spherical symmetry assumption. We however only address the assumptions of thermal and clock noise in this work.

2.4.8 Generating Bending Angle Profiles

Once refractivity profiles are generated from the surface up to around 200 km they are converted to the corresponding refractive index defined as n = (N x 1e-6) +1. Refractive index is then converted to a bending angle via the Abel Transform defined from the formula of Bouguer (Born et al., 1980) assuming spherical symmetry (equation A8). Contrary to Earth, the lack of strong horizontal inhomogeneities in the lower atmosphere and the ionosphere, the spherical assumption is a better approximation for Mars. However, inaccurate estimates of the impact parameter can arise from RO profiles that span large surface areas. Once the profiles for a are generated, the integral is evaluated analytically using a cubic spline fit of the refractivity index as a function of impact parameter. Large horizontal variations can occur if the geometry of the RO profile spans too large of a track. In order to address this issue, we only consider RO profiles that last less than 8 minutes to avoid large uncertainties in the retrieved profiles.

2.4.9 Derived Refractivity

In order to map the uncertainty to physical parameters by using equation 2, the bending angle profiles are translated back to refractivity via the Abel Inversion (Hajj et al., 2002; Tricomi, 1985) (equation A9). The varying noise-added and noiseless refractivity index profiles and the ones varying noise-level added are stored separately for further processing.

2.4.10 Deriving Physical Parameters

Converting the refractivity profiles to density is straightforward, the code simply uses equation 2 to accomplish this. Using a dual frequency approach, X-band for the lower atmosphere and UHF for the ionosphere, the neutral and electron density profiles are resolved separately. Alternatively, the higher Ka-band can be substituted for X-band, and S-band can resolve ionospheric electrons in place of UHF, but this study considers X and UHF bands for simulations. The hydrostatic equation with ideal gas assumption is integrated over all altitudes in order to retrieve a pressure profile from the surface up to the desired altitude. Finally, in order to retrieve temperature profiles, equation 2 is used once more since the refractivity and pressure are known. Utilizing a Monte Carlo method, the numerical code can generate n different realization of noise profiles. The root-mean-square error (equation 3) is computed for each of the physical parameters, where $\hat{y}_I$ is the noise, and y is the truth value over n iterations. The error of the quantity is referenced with our preliminary requirements presented, allowing us to "dial-in" the functional instrument requirements based on state-of-the-art technology for SmallSats.

$$RMSE = \sqrt{\sum_{i=1}^{n} \frac{(\hat{y}_i - y_i)^2}{n}} \tag{3}$$

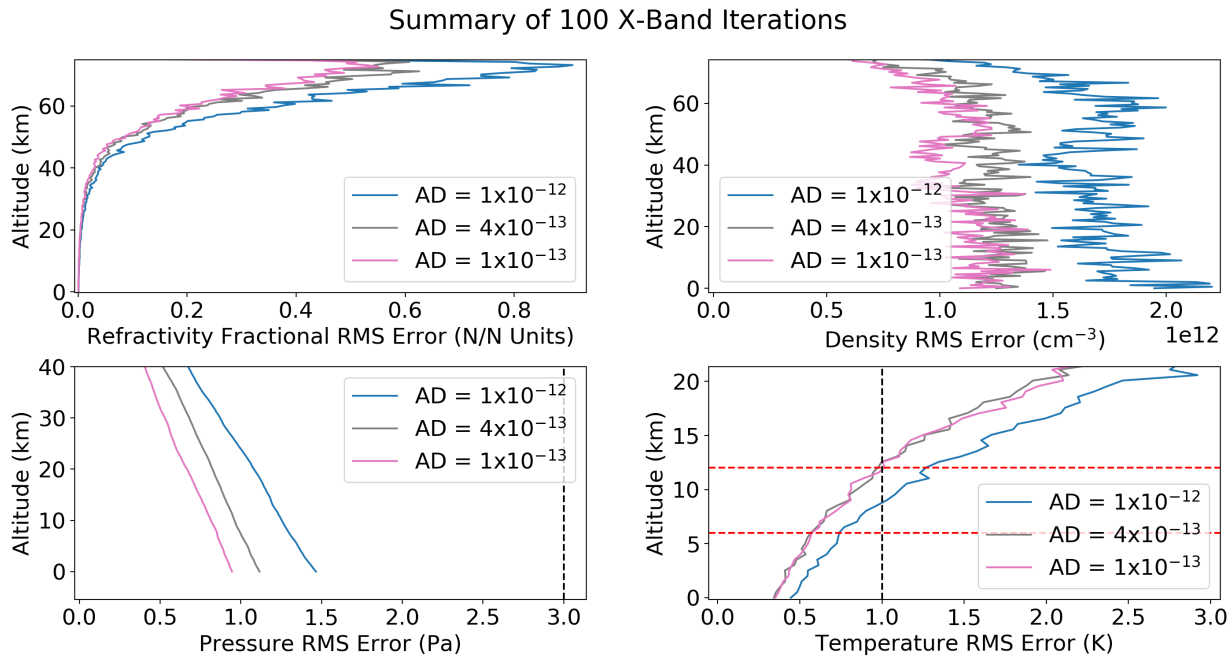

Figure 2.6. Neutral atmosphere uncertainties for X-band derived from 100 Monte Carlo simulations. Each profile is for a different USO Allan Deviation. Vertical black line shows requirement of 1K uncertainty between 6 km – 12 km (red lines).

2.4.11 Ionosphere Simulations

In order to extract realistic electron densities from the upper atmosphere, we utilize a simple Chapman Model as described in (Withers, 2009) to derive realistic electron densities from ~90 km to 350 km above the surface. The peak electron density was initialized at 120 km at a value of 2 x 10^5 cm^{-3}. The Chapman function is dependent on altitude and Solar Zenith Angle (SZA) as illustrated in Figure 2.7.

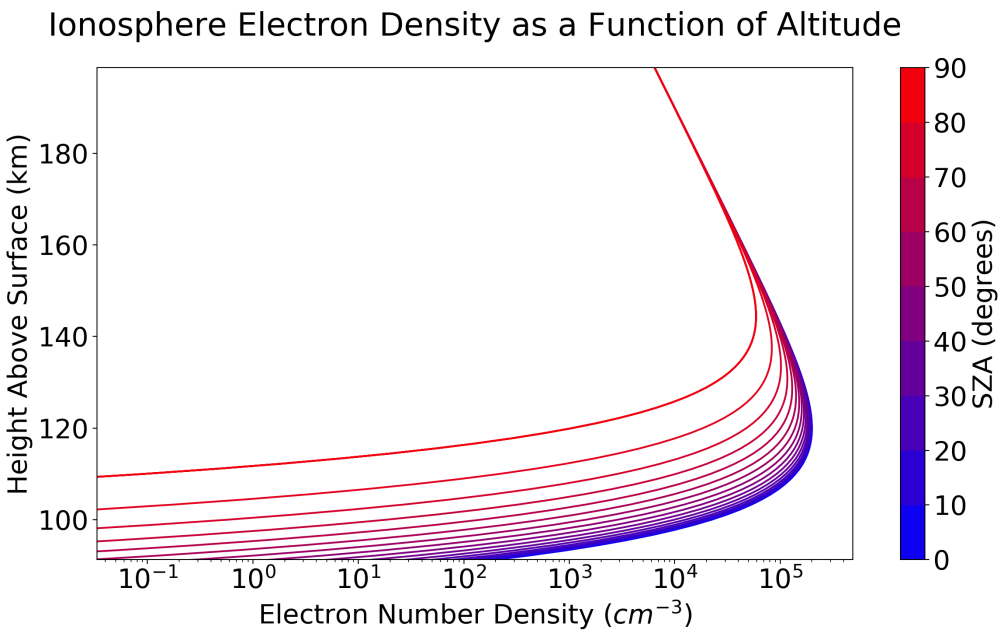

Figure 2.7 Chapman model showing electron density as a function of altitude and SZA with density at ~120 km.

The refractivity in the ionosphere is directly proportional to the radio frequency chosen, and the electron density is described in equation 2. Corresponding noise levels from Table 2.2 for UHF were introduced to determine which ADs meet our preliminary requirements for measuring the ionosphere with ~5% uncertainty (Table 2.1, Objective 2). Figure 2.8 illustrates that the ionosphere is the atmosphere layer most sensitive to thermal noise, thus the varying AD values yield similar results. To achieve the ~5% accuracy (vertical black line) in electron number density, the altitudes are constrained from ~110 km to ~140 km where the density is highest and therefore the region of greatest interest.

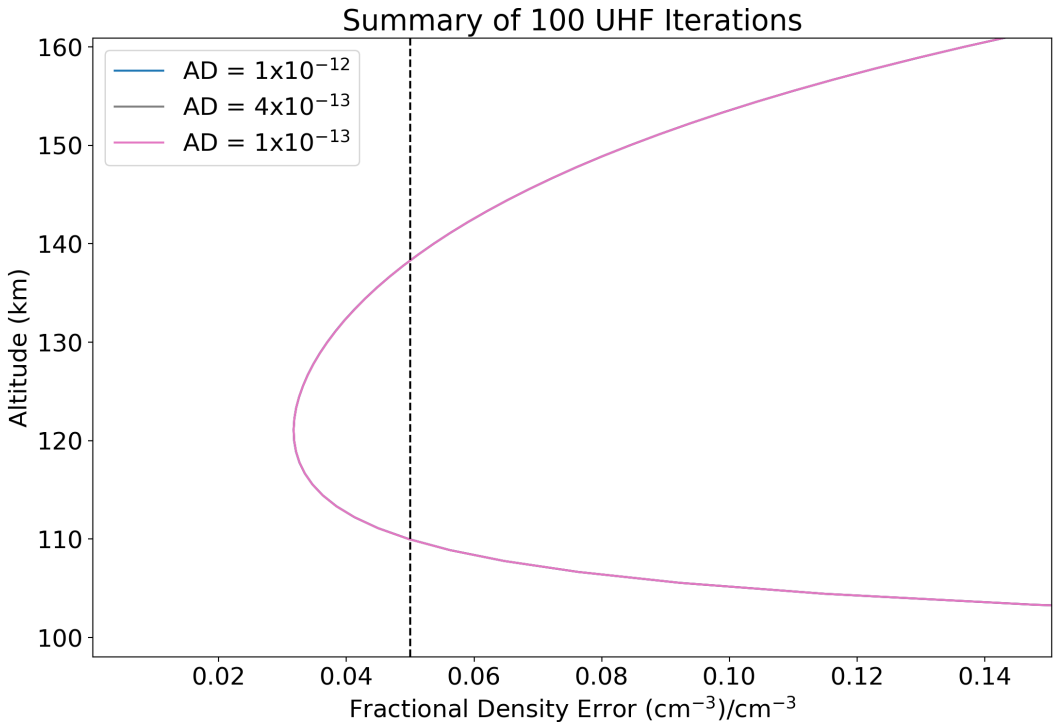

Figure 2.8. Electron number density uncertainties for UHF band derived from 100 Monte Carlo simulations. Each profile is for a different USO Allan Deviation. Vertical black line shows requirement of ≤5% uncertainty

2.5 Summary And Future Work

The focus of our study is the development of a mission concept using SmallSats that can provide unprecedented coverage of RO measurements. We have been developing a framework, tailored to first choosing an optimum orbital configuration, followed by simulating noise values based on specific hardware properties. We are continuing to explore configurations which will provide maximum coverage for the lowest delta-V cost and high revisit time. Thus far, we have identified a possible configuration (configuration 2) with an insertion delta-V of 1.88 km/s with 6 SmallSats. Two are in one orbital plane at 7,000 km with 80° inclination, and four are in one orbital plane at 250 km with 70° inclination. The constellation yields 160 full RO profiles per

day with global coverage and average duration of a full occultation is 330 s. We have also found that the USO capability must meet at least 4 x 10^{-13} s/s to have <1 K temperature uncertainty below 12 km above the surface. Since the ionosphere measurements are not as susceptible to clock noise, future work will involve looking into transceivers and antennas for SmallSats that can minimize thermal noise through higher gains and lower SNRs. This will also allow us to expand the region of the ionosphere that meets the 5% electron density requirement (above 140 km, below 110 km).

Chapter 3

Modeling of Clock and Thermal Noise for SmallSat Radio Occultation Planetary Mission Concepts

This chapter has been submitted for publication: Sweeney, D., Ao, C., Vergados, P., Rennó, N., Kass, D. "Modeling of Clock and Thermal Noise for SmallSat Radio Occultation Planetary Mission Concepts." *Radio Science* (2022): Submitted.

Abstract

Given the advancing capabilities of SmallSat technology and the growing interests in the human exploration of Mars, we investigate the feasibility of obtaining high accuracy radio occultation (RO) profiles with hardware that can be readily implemented for a SmallSat mission. Although RO experiments have been performed between a spacecraft and an Earth ground station since the 1960s, the relatively sparse sampling of these measurements is not sufficient to provide the spatial and temporal coverages needed in many applications. Crosslink RO measurements enabled by a constellation of SmallSats offer a new opportunity to significantly increase the measurement density. A potential challenge towards cost-effective implementation of SmallSat crosslink RO is the need for an ultra-stable oscillator. In this study, we present a new approach adapted from gravity ranging experiments that utilizes dual one-way radio links to

reduce measurement errors from clock drifts. We show that with this approach, a significantly less stable clock can be used to achieve the same accuracy of traditional RO observations, enabling the use of cheaper and smaller clocks in these missions.

3.1 Introduction

Radio occultation (RO) remote sensing measurements have a long flight heritage on planetary science missions, especially at Mars(Hinson et al., 1999, 2014; Tellmann et al., 2013; Vogt et al., 2016; Withers, 2010). Traditionally, tracking the phase of radio frequency (RF) signals from a Deep Space Station (DSN) antenna across a planet's limb to a spacecraft occulting behind a solar system body, we can infer atmospheric properties such as, air density, refractive index, pressure, and temperature. The relative motion between a spacecraft and the DSN allows for the vertical scanning of the planetary atmosphere. Aside from the DSN-to-spacecraft occultations, RO measurements are also performed between two orbiting spacecraft, as has been done in Global Navigation Satellite System (GNSS) RO to sense the Earth's atmosphere since the 1990s (Kursinski et al., 1997), or more recently for Mars at UHF frequencies (Ao et al., 2015; Nava et al., 2020). The observation geometry illustrated in Figure 3.1 shows two occulting spacecraft, S/C A and S/C B, at different altitudes having different velocities together with the ray-path trajectory, which is bent due to changes in the vertical gradient of the air refractivity. The total signal bending is represented by α, and the tangent point (red dot) is defined as the point of the closest approach during an RO. Assuming spherical symmetry, an integral transform can be used to convert the bending angle, α, to atmospheric refractivity (Fjeldbo et al., 1971). Once the refractivity is derived, physical parameters such as pressure, temperature, and number density can be retrieved by assuming the atmosphere behaves as an ideal gas in hydrostatic equilibrium.

Phase measurement errors during ROs due to clock instabilities or drifts onboard the orbiting spacecraft over the occultation time (~1-2 min for Earth-sized planets) limit the accuracy of the retrieved atmospheric parameters (e.g., (Withers, 2010)). The metric used to characterize the clock stability is the Allan Deviation (AD) and is expressed in s/s. Unlike single- and double-differencing techniques of dual-frequency phase measurements that remove all clock errors in terrestrial ROs (Kursinski et al., 1997); Table 3, in planetary ROs where only a single orbiter tracks a single DSN antenna we cannot apply such techniques. Thus, the phase stability onboard spacecraft is vital to enable planetary RO measurements. Historically, Voyager 1 and 2 probed Jupiter's atmosphere during a flyby in 1979 allowing for partial characterization of the ionosphere (Eshleman et al., 1979) used an Ultra-Stable Oscillator (USO) with an Allan Deviation (AD) of 10-12 s/s. In 2006, the European Space Agency Venus Express mission performed over 100 RO partial profiles of Venus' atmosphere with a clock AD of ~3-4 x 10-13 s/s (Tellmann et al., 2013). On Mars, the first orbiter to carry a USO for RO observations was the Mars Global Surveyor (MGS) with an AD of 10-13 s/s over a timescale from 10 to 100 s (Hinson et al., 1999). The Mars Reconnaissance Orbiter (MRO) was the second Mars orbiter to carry a USO with an AD of 10-12 s/s over 10 to 100 s integration time (Hinson et al., 2014). Akatsuki, which is currently the only Venus orbiter that takes RO measurements, has onboard an USO with an AD less than 10-12 s/s at the integration time from 1 to 1000 s (Miyamoto et al., 2014).

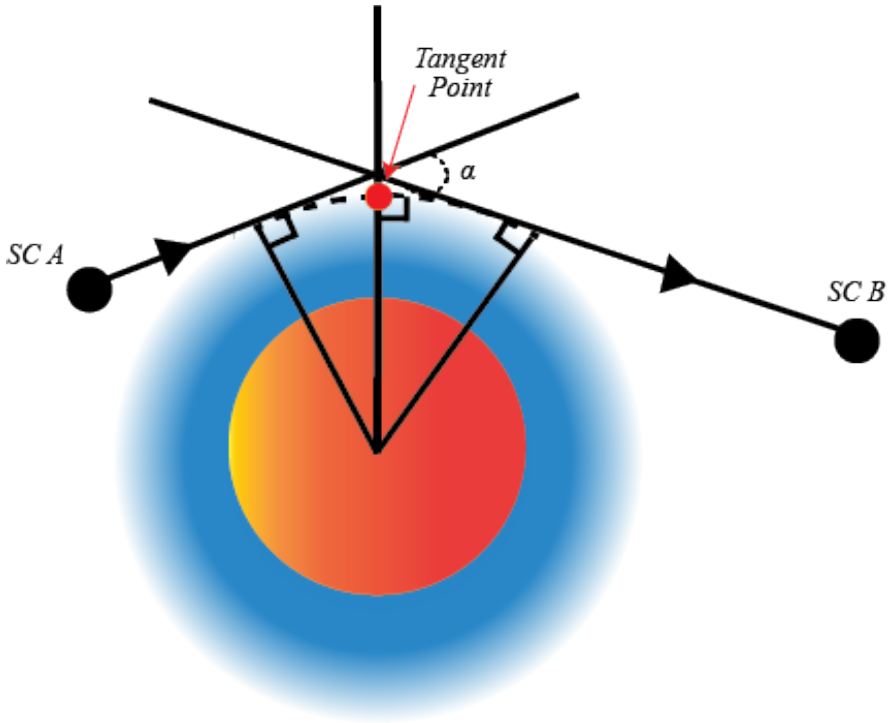

Figure 3.1. Radio occultation between two spacecraft S/C-A and S/C-B. Angle alpha is defined between the two intersection points outside the atmosphere. The Ray path is denoted by black arrows from SC A to SC B. Tangent point (red) is below intersection point, inside the atmosphere. The point moves in a vertical motion dependent on the spacecraft velocities.

Although large flagship interplanetary missions can carry USOs that provide comparable clock stability with the RO missions orbiting Earth, the use of SmallSats as cost-effective solution to study Earth's weather and climate was demonstrated via Spire, GeoOptics, and PlanetiQ. The first demonstration of planetary ROs with SmallSats was attempted on Mars with the MarCO mission (Oudrhiri et al., 2020) carrying a clock with AD of 1.4 x 10-10 s/s over 1 s integration time. Evidently, planetary RO measurements are more challenging to make using SmallSats due to limitations in carrying USOs that provide the required clock stability for ROs (~10-12-10-13 s/s). Although RO measurements can be made without a USO using two-way radio transmissions (Hinson et al., 2014), this approach works only during ingress, introduces additional measurement uncertainty, and increases operational complexity. To avoid the above

mentioned error sources, one-way RO links between a spacecraft and a DSN antennae, or between spacecraft in a constellation geometry via cross-link communication, is a more favorable method. However, the one-way RO links require the spacecraft to carry a highly stable USO, an unrealistic scenario for SmallSats due to volume, power and budget constraints. Motivated by the use of SmallSats for planetary RO measurements, our science objective is to develop a rigorous approach to model the effect of clock noise on RO retrievals between SmallSats that considers the time-correlated characteristics of the noise in the phase of the radio signals. In addition, we describe a new dual-frequency one-way (DOW) method (Thomas, 1999) for RO that enables the use of a less stable clock to achieve the accuracy required by human missions. Such precision for EDL and human exploration is defined in Goal IV, investigation B3.2 of the 2020 MEPAG survey (Banfield, 2020) in terms of temperature of 10-1 Pa precision. Due to lack of near surface measurements of pressure and temperature, current mesoscale models lack this accuracy and precision needed to safely land humans on the surface. The benefits of using a less stable clock results in a more compact payload that could be easily accommodated on SmallSats and are available as commercial off the shelf (COTS) parts for a fraction of the cost of a dedicated payload. The remaining portion of this paper is organized as follows. In Section 2, we outline the new methods which minimize sources of error in RO measurements, and how uncertainties are simulated by a Monte Carlo code. In section 3, we discuss the results of the simulations and the required AD of a clock that can be used in SmallSat RO missions. In Section 4, we highlight the conclusions.

3.2 Methodology

There are several sources of uncertainties in RO measurements that must be properly characterized because RO errors propagate into the retrievals of refractivity, number density,

temperature, and pressure (Kursinski et al., 1997; Withers, 2010). We seek to quantify the key errors that are particularly relevant to a SmallSat RO mission. The measured phase of the signal received at each time during an occultation can be modeled as:

$$\phi_i = \rho + c(dt_A - dt_B) + d_{atm} + N_i\lambda_i + MP_i + \varepsilon_i$$

where ϕ_i is the phase at each frequency *i*, ρ is the geometric range between the spacecraft, c is the speed of light, $dt_A - dt_B$ is the clock error at the transmitting spacecraft minus the clock error at the receiving spacecraft, $d_{atm}$is the atmospheric delay, $N_i\lambda_i$ is a phase ambiguity term, MP_i accounts for multi-path and ε_i is the thermal noise term. The phase ambiguity term is constant during an RO and can be ignored, since only phase rate is relevant. We will also assume that the multi-path term is negligible relative to other terms due to the compact factor of the spacecraft bus. In this study, we focus on the errors arising from the clock and thermal noise terms as they contribute the most to the uncertainty of the received phase signal. These two terms are uncorrelated, and therefore the total error can be expressed as the root square sum (RSS). The clock instabilities are typically characterized by the AD at different integration times which are used to model the expected clock performance. The thermal noise present in the communications system manifests mainly in the form of signal-to-noise ratio (SNR) of the antenna and the receiver. For the thermal noise, a proper link budget is derived (Table 3.1) as a first order approach appropriate for a SmallSat mission. In our previous study (Sweeney et al., 2021), white noise was used to approximate the clock uncertainties based on the AD at a 1 sec integration time. However, this approach neglects correlations in real clock noise, i.e. how noise is not linear throughout the frequency spectrum. Here, we describe an improved method to model the effects of clock noise more properly. This method captures the phase uncertainties as they propagate in

the frequency domain before transforming back to the time domain for the computation of these errors in Doppler shift and physical parameters.

3.2.1 Monte Carlo Simulations of Clock Noise

We use (Barnes et al., 1971) and (Thomas, 1999) clock Power Spectral Density (PSD) to determine the phase noise over multiple time scales given by equation 4:

$$S_\phi(f) = h_0 + \frac{h_{-1}}{f^1} + \frac{h_{-2}}{f^2} + \frac{h_{-3}}{f^3} + \frac{h_{-4}}{f^4} \quad 4$$

where $S_\phi(f)$ is the Single Sideband (SSB) phase spectrum in units of rad^2/Hz and pertains to the base oscillator operating frequency (usually ~ 5MHz). Quartz based USOs are most common for spaceborne applications, but some GPS RO experiments utilize Rubidium or Cesium clocks to derive timetags. However, at small integration times, the clock error ranges from 10^{-11} to 10^{-12}. We will be considering the lowest error quartz based clocks for short integration times for the remainder of the study (Sydnor, 1993). To estimate $S_\phi(f)$ in equation (4), we must first determine the h_n (where n = -1, -2, -3, -4) coefficients using the empirical relationship for the AD at different integration times (τ):

$$\sigma_y^2(\tau) = \frac{1}{f_0^2}\left[\frac{h_0 f_h}{2.565^2}\tau^{-2} + \frac{h_{-1}[2.184 + l(f_h\tau)\,]^2}{2.565^2}\tau^{-2} + h_{-2}\tau^{-1} + 1.665^2 h_{-3} + 3.63^2 h_{-4}\tau\right] \quad 5$$

Here, σ_y^2 is the squared Allan variance, f_0 is the base operating frequency of the oscillator (usually ~5MHz), and f_h is the output oscillator frequency (typically 1 Hz). In equation 5, h_0 is dominant at high frequencies, or low integration times ($\tau < 0.001\ s$). If the smallest AD is

given at 1s, little information can be retrieved about h_0, so this term must be approximated by the noise floor of the oscillator. Additionally, the 1/f term in equation (5) can be neglected for quartz-based USOs (Thomas, 1999); thus we focus on the h_{-2}, h_{-3} and h_{-4} coefficients, which can be solved analytically using matrix multiplication (Appendix A.2). As an example, a GRACE type USO with integration times of 1, 10, 100 and 1000 seconds has ADs of 2 x 10^{-13}, 1 x 10^{-13}, 1 x 10^{-13}, and 2 x 10^{-13}, yielding a PSD function of (Thomas, 1999):

$$S_\phi = 3.16 \times 10^{-16} + \frac{8.38 \times 10^{-13}}{f^2} + \frac{5.74 \times 10^{-14}}{f^3} + \frac{6.39 \times 10^{-17}}{f^4} \quad (6)$$

Through combining equations 4 and 5, a single function (equation 6) can be used to describe the PSD unique to a USO in which noise is generated across the Fourier frequency spectrum. From the PSD, random realizations of noise in time domain can be generated as follows (Thorsos, 1988; Mack, 2013). First, we generate a set of random numbers in the frequency domain:

$$F(f_j) = \sqrt{\mathrm{T} * S_\phi(f_j)} \begin{cases} \frac{(\eta_1 + i\eta_2)}{\sqrt{2}}, & j \neq 0, \pm\frac{N}{2} \\ \eta_1, & j = 0, \pm\frac{N}{2} \end{cases} \quad (7)$$

where t_n is the translated time series in seconds, and $\phi(t_n)$ is the time dependent phase. To translate from the frequency to time domain using FFT, SSB spectrum values must be mirrored in negative frequencies. As an example, Figure 3.2 illustrates three different USO's SSB spectra shown from Fourier frequencies of 0 to 5 Hz equally spaced over 1,000 sample points. The frequency range was deliberately chosen to give a timescale of a typical Mars RO observation. After taking the FFT, this translates to a time averaged sampling of 10 Hz from 0 to 200 s, a typical value for a Mars RO observation (Ao et al., 2015).

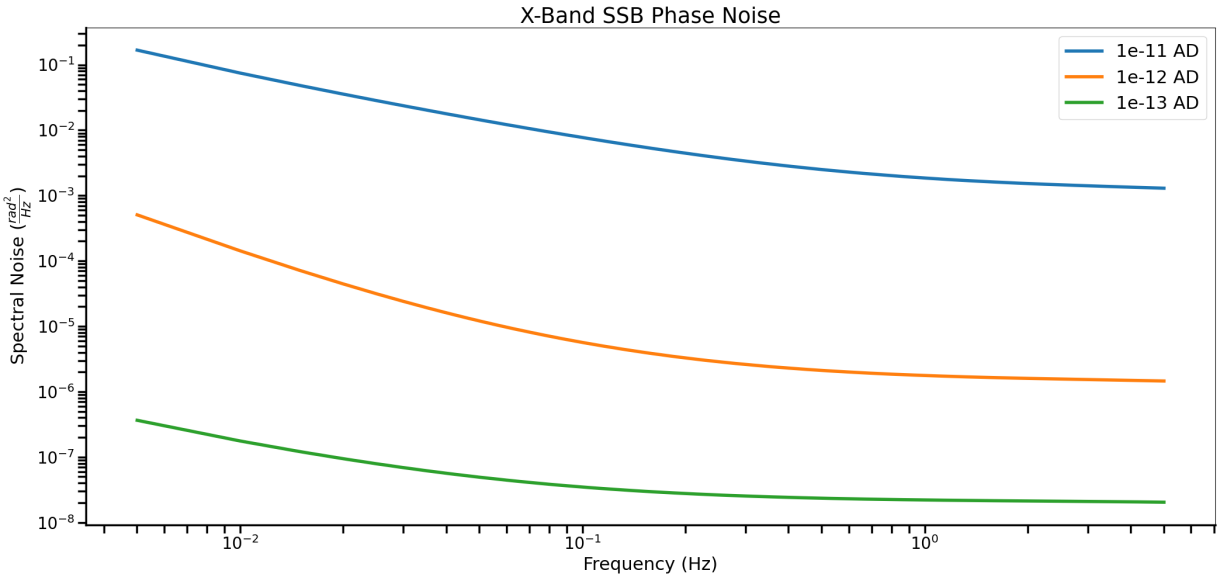

Figure 3.2. SSB of 3 different clocks from 0 to 5 Hz with 1,000 sample points.

The simulations are performed considering one type of clock at a time. Once values are determined for the spectrum, values are mirrored for negative frequencies and the inverse FFT is applied to convert the phase uncertainty into the time domain. The raw signal is sampled at a high rate, but after on board processing, the data is smoothed further using time averaging (e.g., every 10 points for 1 s integration time or 10 Hz) to improve the accuracy of the retrieval. Time averaging of the signal could be performed on board the spacecraft if needed to minimize the amount of data transmitted back to Earth. The frequency range chosen is from -5 to 5 Hz with 2,000 samples. After the initial smoothing of the data, a typical Mars RO experiment with duration of 200 s is obtained. The simulation code performs an iteration of the noise generated PSD and repeats this for a high number of realizations (in this case 100) to obtain a statistically significant sample for the RMS deviation around to the “true” signal.

3.2.2 Dual Frequency One-Way Method

Traditional one-way RO experiments rely on transmitting a single frequency signal from one source to an orbiting spacecraft as it passes into (ingress) or out of (egress) the limb of the atmosphere relative to the signal source. A two-way technique is used when the clock onboard the spacecraft is less stable. In this case, a signal is transmitted from the ground station to the spacecraft, and the signal is transmitted back from the spacecraft to the ground station using the stable uplink carrier signal as a reference. This method has been proven to be effective at sampling Mars' atmosphere as long as the source clock is stable (Hinson et al., 1999). However, a SmallSat mission may not be able to accommodate the size, power, or cost requirements that a high precision USO would require. We propose using a more complex, but also more effective method to accurately determine the clock noise of a less precise USO, in a DOW RO geometry. This method is similar to the approach used in satellite gravimetry like the GRACE and GRAIL missions (Thomas, 1999). In a DOW approach, the two satellites (A and B) participating in an occultation will transmit and receive to each other at the same time, in slightly offset frequencies (to avoid RF interference). The filter is derived through adding the phase of spacecraft A and B. Let us consider only the clock noise component of the phase. Spacecraft A (B) transmits in $\lambda_a(\lambda_b)$, at time τ_0. The clock error term $c_a(c_b)$ is a function of τ, with an additional noise term to account for atmospheric effects ρ. The time to travel from A to B (on the order of ms) is $\Delta\tau$. We can derive an expression for the clock phase received at spacecraft A (B) from B (A)

$$\phi_a = [\Delta\tau + c_a(\tau_0 + \Delta\tau + \rho) - c_b(\tau_0)]\lambda_b$$
$$\phi_b = [\Delta\tau + c_b(\tau_0 + \Delta\tau + \rho) - c_a(\tau_0)]\lambda_a \quad (8)$$

The total clock noise is computed by adding the phases received at both spacecraft A and B.

$$\phi_{total} = \phi_a + \phi_b \quad (9)$$

In adding the phase noise terms, the time derivative is computed by a Taylor expansion about the point τ_0. Assuming the same clock is equipped on both spacecraft, $\dot{c}_a \; and \; \dot{c}_b$ represent the AD over the course of the occultation.

$$\phi_{total} = [\Delta\tau + c_a(\tau_0) + \dot{c}_a(\tau_0)(\Delta\tau + \rho) - c_b(\tau_0)]\lambda_b + [\Delta\tau + c_b(\tau_0) + \dot{c}_b(\tau_0)(\Delta\tau + \rho) - c_a(\tau_0)]\lambda_a \quad (10)$$

To illustrate the self cancellation of the filter, let us consider the AD of the clocks at both transmitting frequency and assume $c_a = c_b$ and if the transmitting and receiving frequencies are in X-Band, $\lambda_a \approx \lambda_b$. Equation 9 can be simplified to

$$\phi_{total} = [\Delta\tau + \dot{c}(\tau_0)(\Delta\tau + \rho)]2\lambda \quad (11)$$

Assuming an AD on board of 10^{-12} s/s, and a transmit time of ~1 ms, the term $\dot{c}(\tau_0)(\Delta\tau)$ in equation 10 is approximated at 10^{-15} s/s, 3 orders of magnitude improvement from a traditional one-way RO experiment. Indeed, by differencing the phase measurements received from Satellite A and Satellite B, the phase noise is largely cancelled if the integration time and distance between the send and receive sources are selected properly (short light time travel) via a frequency filter (Figure 3.3). The simulation code combines the new noise propagation approach outlined in section 3.1 with the DOW method to achieve the same accuracy with a less stable clock on the order of 1 x 10^{-11} s/s from 1 – 1,000 s integration time.

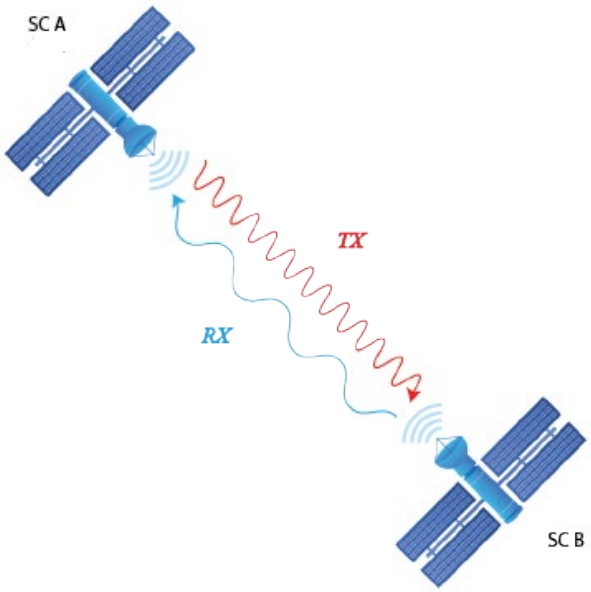

Figure 3.3. Simple illustration of a DOW transmission. SCA is simultaneously transmitting (TX) and receiving (RX) at slightly offset frequencies to match cycles of TX to cycles of RX, effectively cancelling much of the phase error.

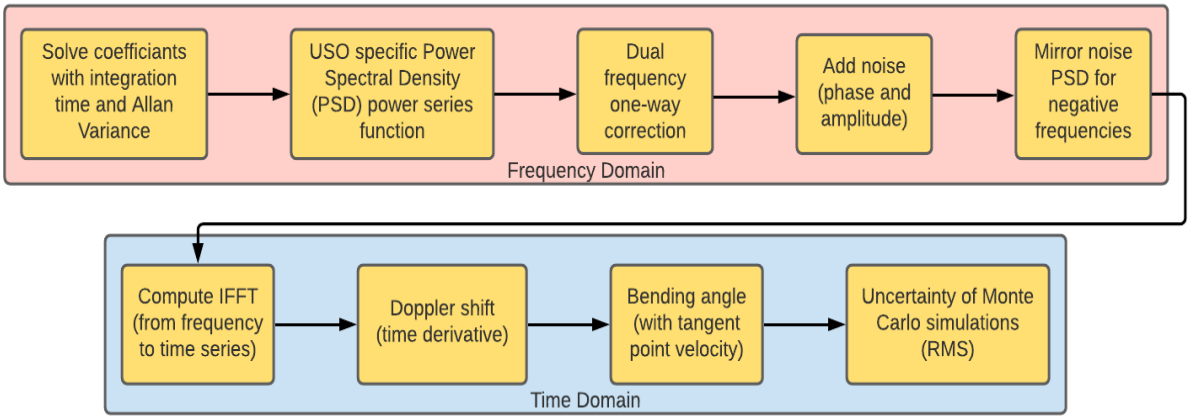

Figure 3.4. Flow down of process starting with Single Side Band (SSB) Power Spectral Density (PSD) spectrum, adding artificial noise in the frequency spectrum, converting to time series phase noise and finally bending angle noise.

To generate the frequency filter, the phase cycles recorded must be matched to one another in post processing onboard the spacecraft, meaning the frequencies chosen must be coherent. The algorithm implemented into the simulation code effectively lowers the overall noise floor and

flattens the spectrum, especially at low frequencies. The filter function is shown to be (Thomas, 1999):

$$\sqrt{G_o(f)} = \frac{\lambda_e}{2}\left|\left(\frac{f_a}{f_b} - e^{-2\pi i f \tau}\right)\right| \qquad 12$$

where f_a and f_b are the transmit and receive frequencies respectively (e.g., $\Delta f = f_a - f_b \sim 500$ MHz for X-Band), f is the Fourier frequency and τ is the transmit time between spacecraft (~0.02 s). λ_e is defined as the effective RF wavelength, and is explicitly accounted for in the calculation of coefficients for the PSD. If the wavelength is omitted from the expression, we assume that cycles are mapped to cycles via the choice of coherent frequencies This makes equation 12 a unitless scalar function that can be applied to the PSD. The first term inside the bracket of equation 11 is a simplified term that accounts for short term RF noise at the receiver and accounts for both spacecraft. The exponential term in equation 12 represents the frequency response given an input Fourier frequency and light time travel value as input. The operational frequency of a USO typically has a value around 5 MHz but depending on the transmitting frequency of the signal, any noise present from the source will be amplified by higher frequencies. The SSB profile is given in rad^2/Hz, so the higher the frequency the larger the noise profile is expected to be. An example in Figure 3.5 illustrates how the PSD changes from the base 5 MHz signal up to X and Ka bands. The figure further illustrates how a DOW filter can be applied (dashed lines) on the same signals to lower and flatten the expected noise in the overall spectrum.

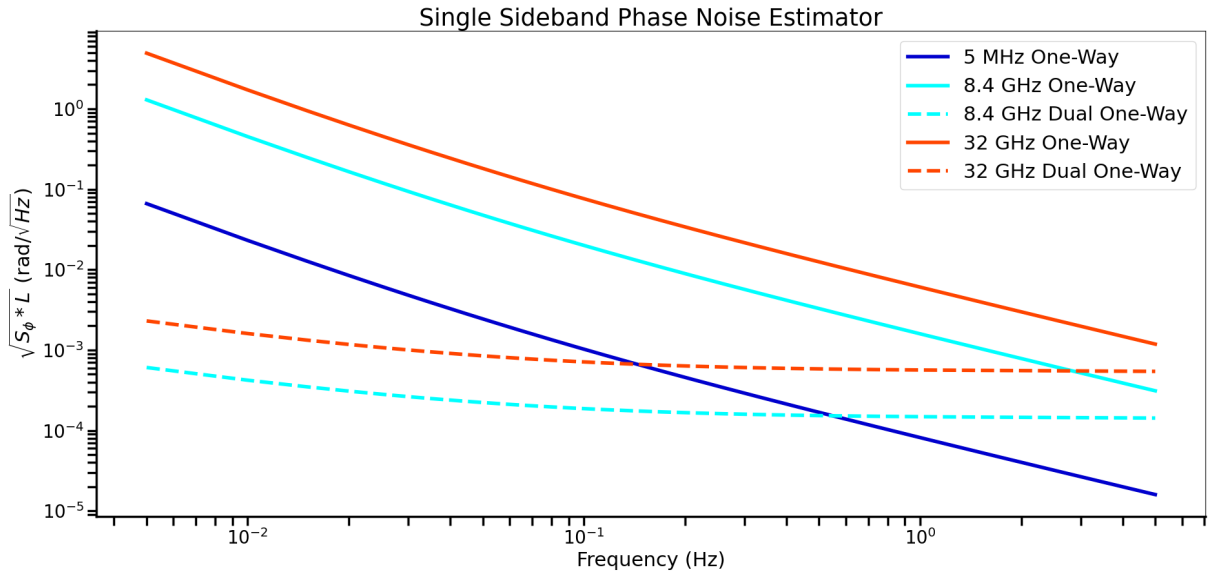

Figure 3.5. Phase noise uncertainty as a function of Fourier frequency (integration time) at 5MHz, 8.4 GHz and 32 GHz frequencies for one way and filter applied DOW methods.

Combining the expressions for the PSD and simplified frequency filter, results in the expression for the SSB

$$S_R(f) = \frac{1}{2}\left|\left(\frac{f_q}{f_p} - e^{-2\pi i f \tau}\right)\right|^2 S_\phi(f) \qquad 13$$

For up-sampled frequencies in X and Ka bands, Figure 3.5 shows an improvement in reducing clock noise up to 4 orders of magnitude at the lower end of the frequency spectrum. The DOW phase filter accounts for all forms of phase noise, so the communications system will also see a reduction of $\sqrt{2}$ thermal noise as a result of averaging over the thermal noise of two different communications systems (Thomas, 1999). This reduction is accomplished by combining two uncorrelated observations ($\sqrt{2}$), then taking the average of the Tx and Rx (1/2) signals, $\sqrt{2}/2$ simplifies to a factor of $1/\sqrt{2}$.

3.3 Results

Our target requirement for an RO mission at Mars requires temperature accuracy of 1 K below 12 km where the parachute is fully deployed during the EDL phase of a lander or rover mission. Previously, we have determined that a USO with AD of the order of 1 x 10^{-13} s/s would be needed to meet this requirement, assuming white noise from the clock (Sweeney et al., 2021). Here we study how the DOW approach RO could use clocks with larger ADs to make measurements of similar accuracy.

3.3.1 One-Way Phase Noise Simulations

In a previous approach to modelling clock noise, we calculated the theoretical bending angle uncertainty based on the AD alone. As a first order approach, assuming white noise for the clock may have been sufficient, but the more rigorous approach used in this study allows the calculation of the noise spectrum for a specific clock and allows the addition of non-dispersive noise in frequency, meaning varying levels of noise are added at different frequencies. Through deriving the PSD required for a GRACE type USO, the Monte Carlo simulation was run as described in section 3.2.2 Phase uncertainty units are converted to length for X-Band wavelength of 3.75 cm. Next, the time derivative at each smoothed data point is determined to evaluate the Doppler shift uncertainty in Hz, and finally the Doppler shift is converted to an overall bending angle uncertainty with a 1 km/s vertical tangent point velocity. This is accomplished using the relationship in equation 14, where σ_α is the bending angle uncertainty (rad), λ (m) is the wavelength, v_{tpz} (m/s) is the tangent point velocity and $\sigma_{Doppler}$ (Hz) is the Doppler uncertainty (Sweeney et al., 2021).

$$\sigma_\alpha = \frac{2\pi\lambda}{v_{tpz}}\sigma_{Doppler} \qquad 14$$

The PSD is converted to give bending angle uncertainties on the order of $1x10^{-7}$ radians as shown in Figure 3.6. Over 100 iterations, the Root-mean-square error (RMSE) over the 200 second time interval is 6.37×10^{-8} radians, which is close to the original white noise estimation from (Sweeney et al., 2021) of 4.24×10^{-8} radians. Next, we explore the same approach but including a DOW filter in the simulation.

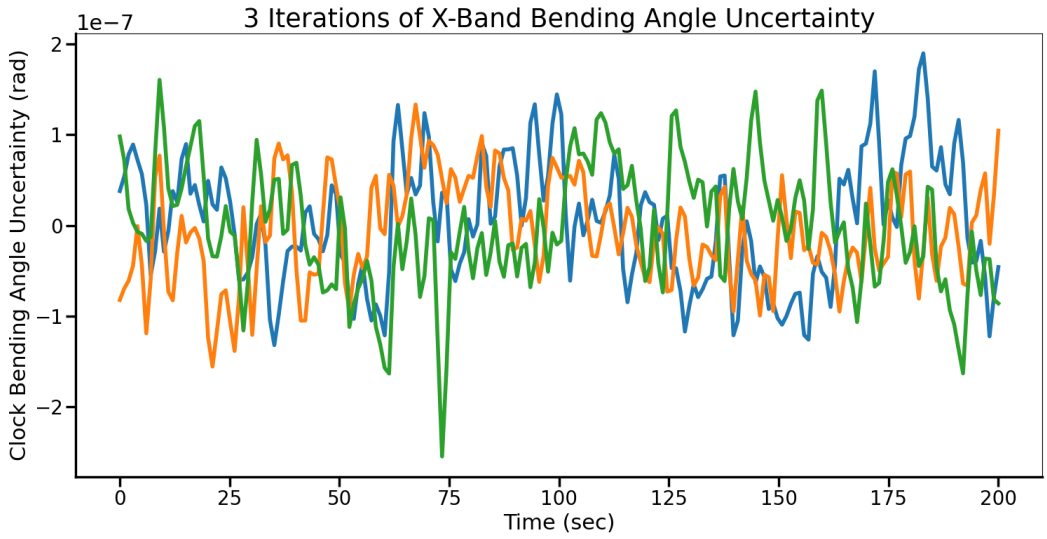

Figure 3.6 Phase uncertainty in radians as a time series generated by taking the inverse FFT of the phase vs frequency data with 3 iterations of noise.

3.3.2 Dual One-Way Noise Simulations

Since a more rigorous approach to modelling clock noise has been implemented, we test the effectiveness of the DOW filter. The results of the full simulation presented in the flow-down (Figure 3.4) was ran for 100 iterations of noise added values with the frequency filter representing the DOW RO derived bending angles. Based on the performance of the filter shown in Figure 3.5 we expect an improvement of up to 2 orders of magnitude in bending angle noise.

Smoothing down to 1 Hz for a 200 s time interval, the RMSE bending angle is shown in Figure 3.7 with a mean RMSE of 7.08 x 10^{-10} radians. This result shows that using a DOW filter on the same USO gives an average improvement by two orders of magnitude. We conclude that using a less stable clock is a viable option for a SmallSat mission. However, with the reduction of clock noise, thermal noise becomes a significant driving factor. In the next section, we will estimate the bending angle and temperature uncertainty with the addition of thermal noise.

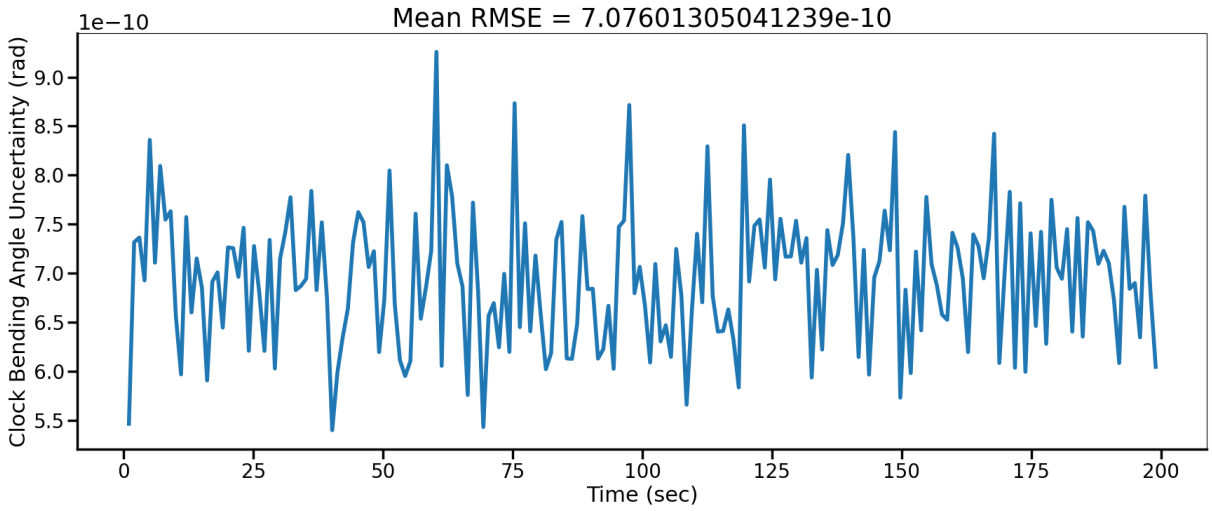

Figure 3.7. Applying a frequency filter for a DOW simulation of 100 iterations of noise smoothed from 10 Hz to 1 Hz.

3.3.3 Thermal Noise Estimates

Thermal noise introduced via the communications system is the second main source of noise which must be characterized fully as it feeds directly into RO retrievals. Uncertainties in transmitted radio signals can be qualitatively modeled as the decoding of a transmitted signal by knowing where a cycle has ended and another has begun. This can be thought as an uncertainty in amplitudes of the transmitted radio signal measured, which is proportional to the square root of the measured power (Withers, 2010). An additional benefit of a DOW RO experiment is that it reduces the thermal noise by a factor of $\sqrt{2}$ since the random noises from the two one-way radio

links are essentially averaged together. To reduce the thermal noise further, we rely on improvements of the SNR with the use of higher gain antennas as shown in the link budget in Table 3.1. The thermal uncertainty can be calculated from equation 15 (Withers, 2010)

$$\sigma_{\text{thermal}} = \frac{\sqrt{\frac{2BN_0}{C}}}{2\pi\tau_{\text{thermal}}} \quad 15$$

where N_0 is the noise power density (W Hz^{-1}), C is the signal power (W), 2B is the noise bandwidth (Hz) and τ_{thermal} is the integration time (s).

The specs for the transceiver are derived from Iris V2.1, which has heritage on the MarCO mission. With a high gain patch antenna in X-band (8.35 dBi) and a lower noise bandwidth of 50 Hz, the total bending angle uncertainties for thermal noise are ~3 orders of magnitude larger than the reduced clock noise from the DOW method for ADs on the order of 7 x 10^{-11} or better. Figure 3.9 shows the total bending angle uncertainty of thermal and clock noise for different types of RO experiments as a function of AD. The 1 K uncertainty required between 6-12 km above the surface is illustrated as a horizontal red dashed line (from Figure 3.8). Even though the total noise is dominated by the thermal component, the 1 K requirement can still be met using the DOW method with a clock characterized by a 3 x 10^{-11} AD.

Parameters	Value	Notes
Transceiver		Iris V2.1
RF Power (dBm)	45.4	
Antenna Gain (dBi)	8.35	Patch Antenna

Circuit Loss (dB)	-0.5	
Total (dB)	53.3	
Path Parameters		
Space Loss (dB)	-186.96	
Range (km)	6,334	Outer to Inner Spacecraft
Wavelength (cm)	3.75	X-Band

.

Table 3.1. (top) parameters used for calculating the signal-to-noise (SNR) ratio assuming a patch antenna, Iris V2.1 transceiver and a higher gain patch antenna. (bottom) parameters used for calculating the SNR and converting it to atmospheric bending angle uncertainty for a DOW RO experiment after multiplication by a factor of $1/\sqrt{2}$ to account for both communications systems.

Thermal Noise for Dual One-Way (X-Band)	
Power (W)	35
Noise Bandwidth (Hz)	50
SNR (C/N_0, dB Hz)	51
$\tau_{thermal}$ (s)	1
Thermal Uncertainty (mHz)	4.49
Thermal Uncertainty (bending angle, rad)	1.13E-07

3.3.4 Total Noise Estimates

We ran 100 Monte Carlo simulation iterations of 6 different levels of atmospheric bending angle uncertainties using our previous code. Since the thermal noise is fixed as it is dependent on the communications systems, the stability of the clock must be characterized through simulations. These simulations were done with a fixed parameter for thermal noise (1.13 x 10^{-7} rad) as calculated in Table 3.1, so only different ADs contribute to the bending angle

uncertainty. These simulations allow a more direct link between expected clock performance required to meet the 1 K uncertainty from the surface to 12 km altitude. Figure 3.8 indicates that the maximum allowable total atmospheric bending angle is 2.5 x 10^{-7} radians.

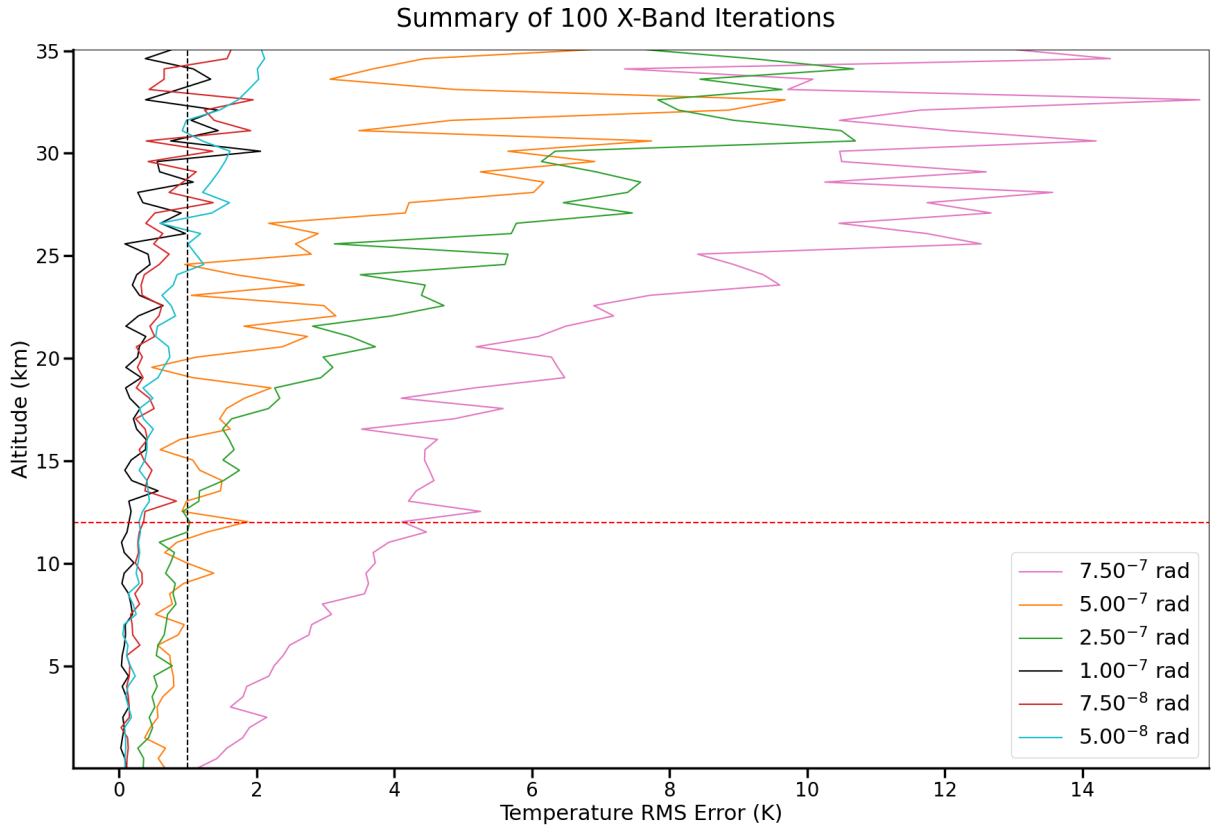

Figure 3.8. Summary of 100 iterations of simulation code for expected amount of temperature uncertainty as a function of altitude and bending angle.

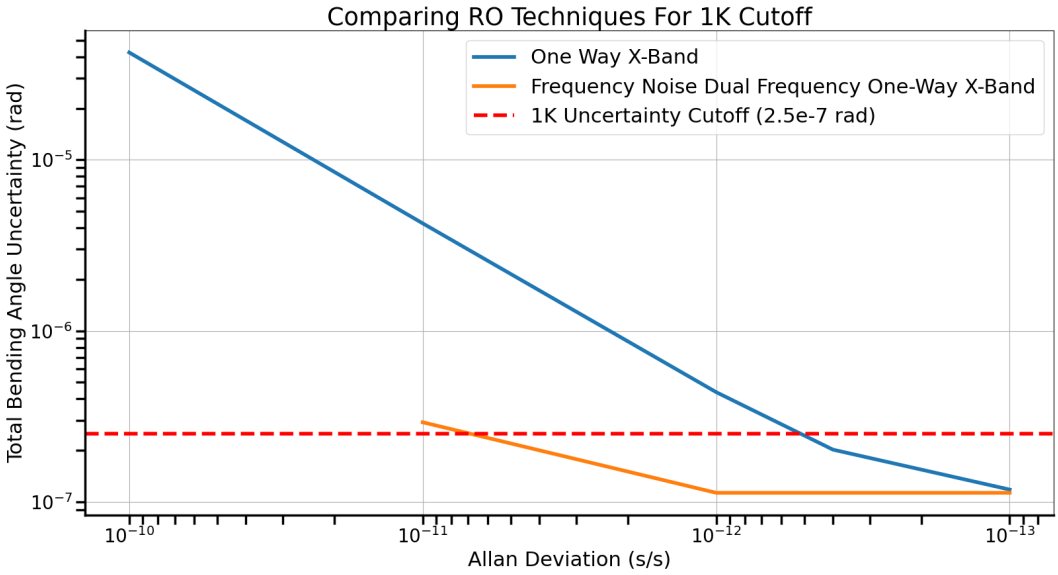

Figure 3.9. Comparison of effective AD in one way and DOW RO experiment in X-Band frequency. The bending angle uncertainty is a function of the AD. Red dashed line shows requirement of 1 K uncertainty for our mission between 6-12 km above the surface.

Finally, by combining all aspects of the full simulation code, 100 iterations of bending angles were conducted for noise types of three different USO ADs, two for the traditional one-way, and three for DOW phase derived noise combined with the thermal component in the previous section. The plots in Figure 3.10 illustrate each parameter derived, that is: refractivity, pressure and temperature uncertainty as a function of altitude. The mission requirement derived for RO to support EDL operations in (Sweeney et al., 2021) states that between 6-12 km above the surface, temperature retrieval uncertainty shall not exceed 1 K. A DOW to RO experiments can meet this requirement with a USO with traditionally low AD of 1 x 10^{-12} (grey line). When comparing this result with the one-way AD of 1 x 10^{-12} (orange line), we observe that the retrieval uncertainty reaches 1 K at several points below 12 km altitude. The middle plot in Figure 3.10 shows the traditional one-way RO retrieval for that a USO with AD of 1 x 10^{-12} exceeds the uncertainty of 1 Pa at the surface, where all DOW retrievals achieve uncertainty

lower than 1 Pa. There are points in the vertical profiles at which a system with AD of 1 x 10^{-12} seem to perform better than 1 x 10^{-13}, but this is to be expected when comparing uncertainties from Figure 3.9. The floor of the DOW filter has the same effect on ADs of this magnitude, so any difference is introduced by random noise.

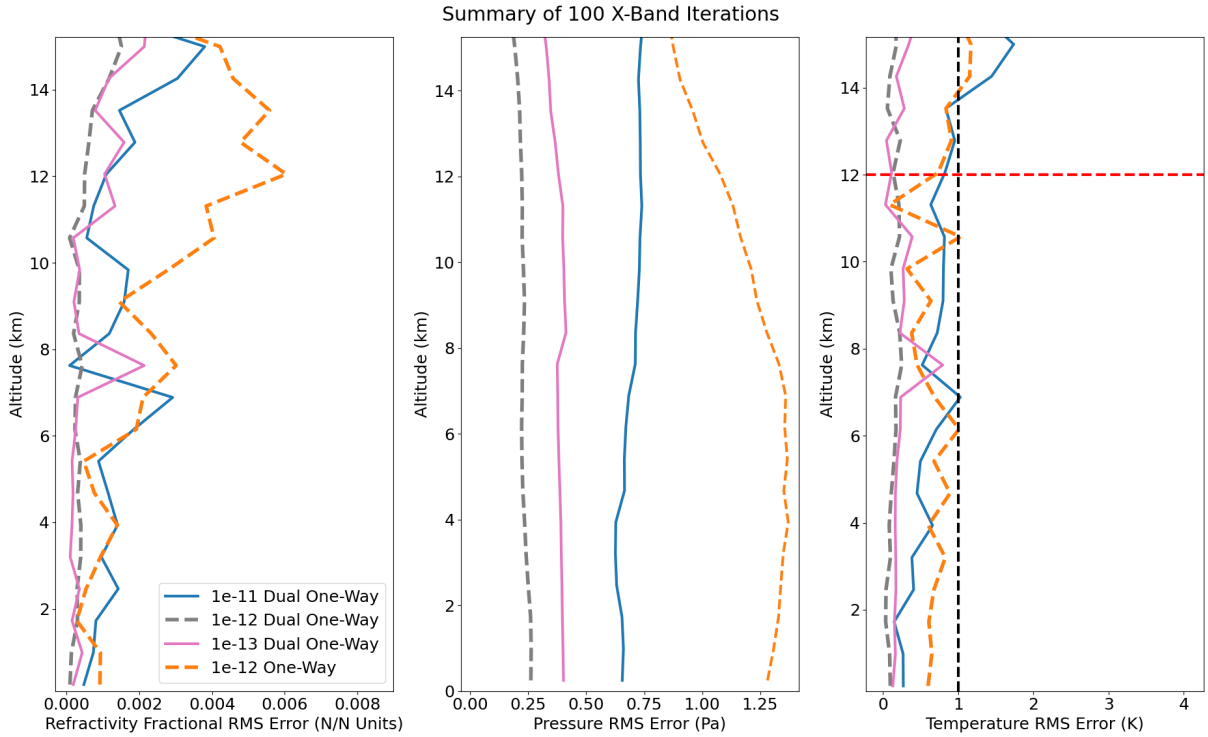

Figure 3.10 100 iterations of different AD's for one-way and DOW generated noise for physical parameters of refractivity, pressure and temperature uncertainties as a function of altitude. The red dashed line in far right figure shows the 12 km cutoff to determine the black dashed line (requirement) of 1 K uncertainty. The most improvement comes from an AD of 1 x 10^{-12} for DOW when comparing the dashed grey line with the dashed orange line.

3.4 Conclusions

Given the growing interest in SmallSat technology for deep space missions, we use a previously developed method to reduce uncertainties in RO experiment retrievals. Sources of noise that propagate into RO retrievals mainly stem from clock noise in the USO and thermal

noise from on board electronics. In our previous study, a first order approach for characterizing clock noise was tested by adding white noise directly in the time domain. Expanding upon this idea, here we use a more rigorous approach by adding noise to the frequency spectrum before translating it into the time domain. Our results yield noise on the same order of magnitude as the simpler approach. However, in our previous study we concluded that a high precision clock with AD of the order of 1×10^{-13} s/s was required to meet our requirements. Clocks with this precise are not feasible for SmallSat missions because of budget, volume, and power constraints. By applying a DOW frequency filter, transmitting at two slightly offset frequencies, much of the phase noise (thermal and clock) can be mitigated. This allows the requirements of 1 K uncertainty near the surface necessary to support EDL operations to be met with a less precise clock with AD of 1×10^{-12} s/s.

Chapter 4

Mars Atmospheric Radio Occultation (MARiO): CubeSat Mission Concept for Atmospheric Remote Sensing

This chapter has been submitted for publication: Sweeney, D., Free, R., Ao, C., Vergados, P., Rennó, N., Cutler, J., et. al, (2023). Mars Atmospheric Radio Occultation (MARiO): CubeSat Mission Concept for Atmospheric Remote Sensing. . *2023 IEEE Aerospace Conference.*

Abstract

The low density of Mars' atmosphere makes the planet vulnerable to dynamic influences from the solar wind, though it is still able to support clouds and seasonal variability. The Martian atmosphere is sufficiently dense to damage any landing spacecraft via heating and aerodynamic forces, though it can also be used as an asset to slow incoming satellites through aero-breaking and other orbital maneuvers. Altogether, future Mars missions, which include stages such as orbital capture and EDL (Entry, Descent, and Landing), will need to overcome complex challenges to navigate and survive this region. Characterization of the Martian atmospheric environment is crucial for informing immediate scientific understanding but also future human exploration activities on the red planet. This report presents the mission concept for the Mars

Atmospheric Radio Occultation (MARiO) mission. MARiO seeks to address these issues by characterizing atmospheric pressure, temperature, and density profiles in the Martian environment through a constellation of CubeSats. To better understand the history and processes surrounding the Martian climate, MARiO will utilize a novel approach to radio occultation (RO) as the primary scientific instrumentation to obtain necessary measurements. Through utilization of a dual frequency one-way approach, simulation results show a CubeSat can achieve the same accuracy as traditional RO experiments at a fraction of the cost. In addition to RO, the Mars Electrostatic Discharge Spectrometer (MEDS) shall detect evidence of electrostatic discharge (ESD) events in the Martian atmosphere. Understanding these ESD events will improve health and safety of both sensitive electronic equipment and astronauts.

4.1 Background

Radio Occultation (RO) is a limb-sounding remote sensing technique that takes advantage of the radio frequencies of the communications system to measure excess Doppler shift caused by the atmosphere, if the composition of the atmosphere is known. RO has a long-standing heritage with interplanetary missions, starting with Mariner IV at Mars in 1965 (Fjeldbo et al., 1965). Traditionally, RO experiments are conducted using an orbiting spacecraft and a ground based Deep Space Network (DSN) station. Relative to the ground station, the spacecraft will occultate the atmosphere inwards (ingress) or outwards (egress) and the carrier signal phase is measured. After accounting for the orbit of the spacecraft, excess Doppler shift in the phase can be converted to the refractivity, as described above. However, these RO experiments are infrequent in number and we do not have enough observations to capture the seasonal and diurnal variations from the near surface to the top of the ionosphere. This data would prove crucial to influence mesoscale models that engineering teams at the Jet Propulsion Laboratory

(JPL), utilize to safely land spacecraft on the surface during the Entry Descent and Landing (EDL) phase. We present a mission concept that employs CubeSat spacecraft to take dedicated RO measurements at all latitudes at a frequency which will characterize the seasonal and diurnal cycles over one Mars year.

Electrostatic discharge (ESD) presents an unknown risk to humans on the surface. Strong electric potentials are created when dust is lifted to high altitudes in the atmosphere during the summer global and regional dust storms (Kok & Rennó, 2006), and evidence of electrostatic discharge has been detected as a broadband signal from Mars based communications signals (Ruf et al., 2009). As a secondary science payload, we include an instrument to detect these broadband signals over the X and UHF (Ultra High Frequency) band signals used for RO in order to pinpoint the originating locations of ESD and evaluate the risk to surface based missions.

4.2 Motivation & Science Traceability

EDL is the most dangerous phase of any surface mission on Mars as fast varying atmospheric conditions could lead to loss of the spacecraft. As of now, engineering teams at JPL use mesoscale models, initialized by global models, to plan for mission success at the intended landing sites (M. Golombek et al., 2017; M. P. Golombek et al., 2003; Kass et al., 2003; Tamppari et al., n.d.) However, if enough RO profiles are obtained for proper input from a dedicated mission, this would lead to improvement of the models used. Given recent interest in SmallSat technology for deep space missions, such as MarCO (Mars Cube One) (Schoolcraft et al., 2016), it has been proven that such mission architectures are possible in the deep space environment. We propose a dedicated constellation of CubeSats as a low-cost alternative to achieve high spatial and temporal resolution to aid in characterizing the Mars atmosphere of over

the course of one Mars year. We introduce a dual one-way frequency method used in past gravity ranging experiments, such as the Gravity Recovery And Climate Experiment (GRACE) (Thomas, 1999), to enhance the accuracy of our measurements which would otherwise rely heavily on a large and expensive Ultra-Stable Oscillator (USO).

The Mars Exploration Program Analytics Group (MEPAG) is responsible for establishing the science goals and objectives for future Mars exploration activities. The 2020 MEPAG report (Banfield, 2020) serves as the basis for creating the overall science objectives of the MARiO mission. There are two specific science goals that the mission will address: (II) understand the process and history of climate on Mars and (IV) prepare for human exploration. In regards to goal II, the mission aims to characterize Mars' atmosphere, with particular emphasis on tracking variability over both diurnal and seasonal timescales. The mission will add to an understanding of the climate variability by measuring diurnal variability of pressure and number density, as well as ionospheric electron number density variability due to interaction between the solar wind and the induced magnetic field of Mars. Two goals for objective II can, around therefore be directly addressed by RO observations. They are 1) to characterize the structure of the Martian atmosphere and 2) to determine the cyclic and seasonal variability in the Martian atmosphere. In pursuit of goal IV, the mission aims to characterize atmospheric factors in order to inform future EDL efforts. This is achieved through continuous vertical profiles of pressure, temperature and number density at all latitudes and local solar times. The science justification for the MARiO mission is presented in Figure 4.1.

4.3 Investigations: Measurements and Instruments

4.3.1 Radio Occultation

For one-way crosslink RO experiments, both spacecraft must have an accurate RSO on board. The Doppler shift can be first converted to a bending angle, then through the use of an Abel transform to a refractivity. Refractivity (N) has a direct correlation to pressure (P) and temperature (T) in the neutral atmosphere, and a frequency (f) dependent relationship to electron number density (n_e) in the ionosphere (Fjeldbo et al., 1971), as seen in equation 16.

$$N = 1.306\frac{P}{T} - 40.3 \times 10^6 \frac{n_e}{f^2} \quad 16$$

Pressure profiles, in particular are retrieved through a combination of the hydrostatic balance equation with the ideal gas law. If two frequencies are used, a linear combination of equation 16 can be used to separate the neutral atmosphere from the ionosphere. However, USOs capable of achieving highly accurate results for a one-way experiment are costly and cannot realistically fit inside of a CubeSat bus. We introduce a method common to gravity ranging experiments, called dual frequency one-way. This method allows for use of a less stable USO by simultaneously transmitting and receiving coherent radio signals to effectively remove phase noise. This frequency filter is applied to the phase spectrum of any USO as referenced in (Thomas, 1999)

$$S_R(f) = \frac{1}{2}\left|\left(\frac{f_a}{f_b} - e^{-2\pi i f \tau}\right)\right|^2 S_\phi(f) \quad 17$$

where f_a and f_b are the transmit and receive frequencies respectively, f is the Fourier frequency and τ is the transmit time between spacecraft (~0.02 s). $S_\phi(f)$ is the original phase noise profile as a function of Fourier frequency and $S_R(f)$ is the reduced phase noise profile. To show the full effectiveness of the method, Figure 4.2 depicts varying USO accuracy's by the Allan Deviation (AD) in units of s/s, from low stability (10^{-10}) to high stability as seen in past RO experiments

(10^{-13}) for X-Band. The red dashed line corresponds to the total bending angle uncertainty between 6-12 km above the surface in order to meet 1K uncertainty for the mission. An one-way RO experiment would need a clock on the order of 5^{-13} s/s while a dual frequency one-way filter can use a much less stable clock on the order of 2^{-11} s/s to achieve the same bending angle uncertainty. A clock of this stability is considerably smaller and capable of fitting on a 6U CubeSat bus.

Legend	
	Related to RO instrumentation
	Related to ESD instrumentation

MEPAG Top-Level Goals	Top-Level Science Objectives	Sub-Objectives	Observables & Physical Parameters	Measurement Methods & Instrumentation Requirements
Prepare for Human Exploration on Mars (MEPAG 2020 Goal IV)	Develop understanding of Mars sufficient to enable human landing at potential sites (4A)	Characterize atmospheric factors affecting orbital capture and EDL for human scale missions to Mars (4A1)	- Spacecraft drag through atmospheric profile (pressure, temperature, density) - Dust storms and related activity	**Radio Occultation (RO)** - 500m vertical resolution -Typical T error of 0.5K -1-2% pressure precision UHF and X bands for separation of neutral atmospheric refractivity from ionospheric refractivity. Heritage frequencies: - UHF @ 437.1 MHz - X-band @ 8.425 GHz ---------- **Mars Electrostatic Discharge Spectrometer (MEDS)** - X and UHF band measurements taken of ESD events in lower atmosphere - Along line of sight of RO opportunities - Minimum time resolution 1s - Desired frequency resolution 0.5 MHz - Data products in format of timeseries domain power & kurtosis spectra, and frequency domain power & kurtosis spectra
			- Frequency and strength of ESD events	
	Develop understanding of Mars sufficient to enable human surface exploration and EVA (4B)	Assess the occurrence, variability of dust storms in the human exploration zone (4B3)	- Cyclical seasonal effects - Dust storms and related activity	
		Assess landing-site characteristics and environment related to safe operations and trafficability during human missions (4B4)	- Atmospheric profile (pressure, temperature, density) - Dust storms and related activity	
			- Frequency and strength of ESD events	
Understand the Processes and History of Climate on Mars (MEPAG 2020 Goal II)	Characterize the Structure of the Martian atmosphere (2A)	Determine thermal structure, and distributions of dust, water, and carbon dioxide in the lower atmosphere (2A1)	- Thermal atmospheric profiles	
		Determine frequency and magnitude of local and global dust storms (2A2)	- Dust storms and related activity	
		Determine temperature, pressure and density profiles of the atmosphere (2A3)	- Atmospheric profile (pressure, temperature, density)	
	Determine cyclic and seasonal variability in the Martian atmosphere (2C)	Determine diurnal variability of the Martian atmosphere (2C2)		
		Determine seasonal variability of the Martian atmosphere (2C2)		

Figure 4.1 MARiO RO Science Traceability Matrix (STM) to support MEPAG top-level goals II and IV.

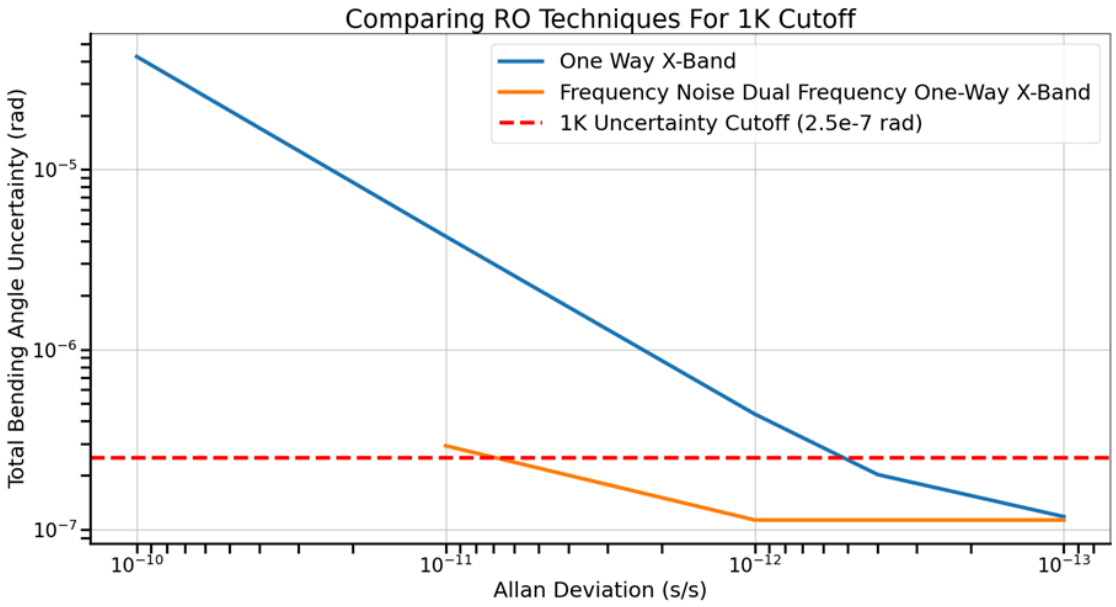

Figure 4.2 One-way and dual frequency one-way as a function of Allan Deviation (AD) and total bending angle uncertainty with a red dashed line showing the 1K uncertainty cutoff required for the mission.

4.3.2 MEDS: Mars Electrostatic Discharge Spectrometer

The Mars Electrostatic Discharge Spectrometer (MEDS) shall be designed in partnership with JPL. Its design shall be based on existing ESD instrumentation utilized in conjunction with the DSN radio based out of Madrid and Goldstone. Ground-based methodology has been developed using the DSS-65, DSS-63, DSS-55, and DSS-54 radio antenna to detect evidence of ESD in the Martian atmosphere. The spectrometer receives signals centered on 8 GHz with a bandwidth of 500 MHz, and is capable of simultaneously processing up to 4 independent radio frequency signals with 2 ms time resolution, used with ground-based measurements for Mars signal confirmation or veto. The instrument utilizes the DSN Mars observations to filter out orbiter transmissions and utilize the remaining atmospheric data for analysis.

The instrument also calculates kurtosis from the spectral power, which is a statistical tool more sensitive to non-thermal perturbations than thermal events, and is, therefore well-suited to identifying ESD events. The kurtosis estimator is calculated in Equation \ref{eq:kurtosis}. The kurtosis is the ratio of the instantaneous

power spectral density (S_2), to the squared spectral power density (S_1) multiplied by the number of instantaneous power estimates (M). This measures the "tailedness" of the distribution, revealing outlier data of surface-originating electric discharge events on Mars.

$$\hat{V}_k^2 = \frac{M}{M-1}\left(\frac{MS_2}{S_1^2} - 1\right) \qquad 18$$

For the MEDS instrument, an adapted version of this spectrometer for use aboard MARiO, the input shall be taken from the Radio Occultation X-Band and UHF signals. Simultaneous analysis of both ranges will be useful in characterizing the emissions, since we expect ESD events to be broadband in nature.

Several architecture options are available for analysis of resulting data products, which include both the processed RO signal and the calculated kurtosis. In previous experiments, four or five hours' worth of observations from the DSN resulted in the order of dozens of GB of data. Relying solely on the CubeSat's own communications architecture, it may be unfeasible to transmit all the ESD data with the RO data. However, with a data relay architecture option, as will be discussed later, this is a possibility.

The other retrieval solution is to process the data with each CubeSat's on-board computer, and transmit only flagged results, thereby significantly reducing the data load. The currently developed detection algorithm is computationally intensive, however, further software development can reduce this to a reasonable CubeSat capability. This on-board analysis can also

search for Schumann resonances (between 7-14 Hz) by performing Fast Fourier Transform (FFT) around flagged events and report these occurrences. Processing data on-board will significantly reduce the MEDS transmit data load. For example, on a five-hour dataset, ESD candidate processing reduced a potential occurrence to a 10-min window.

Further work shall be done to refine the existing ESD DSN spectrometer to a miniature spectrometer version for integration within the MARiO CubeSat design. Other current work includes use of the Allen telescope to attempt to detect ESD, the team for which also developed an FFT analysis spectrometer instrument for use with ground-based measurements (Anderson et al., 2012).

4.4 Mission Concept

4.4.1 Top Level Requirements

The Top-Level Requirements, detailed in Table 4.1, are the functional requirements and constraints imposed on MARiO for mission success. All requirements shall be verified and validated throughout the systems engineering axiomatic design process. All the other system and subsystem-level requirements, included in the appendix, flow down directly from the Top-Level Requirements.

Table 4.1 Top-Level Requirements for the MARiO mission.

ID	Requirement Name	Requirement Description
TLR-1	RO Occultation	The mission shall obtain Martian atmospheric profile measurements via radio occultation (RO).
TLR-2	RO Vertical Resolution	RO measurements shall have a maximum vertical resolution of 500 m.
TLR-3	Global Coverage	The mission shall obtain RO measurements with 10%

		(TBR) planetary coverage per sol, measured through 15 x 15 degree longitude and latitude grids of surface area.
TLR-4	Revisit Time	The mission shall obtain RO measurements with a minimum revisit of 8 times per Martian year (TBR).
TLR-5	Satellite Number	The mission shall deploy a constellation of 2 satellites in orbit around Mars.
TLR-6	Environment Survivability	The mission satellites shall function for the mission lifetime (1 Martian year) at a maximum radiation level of 2000 rads and at a minimum temperature of 3 Kelvin.
TLR-7	Cost	The mission costs shall not exceed $200 million USD with $50 million margin.
TLR-8	Operational Lifetime	The mission shall be in operation for a minimum of one Martian year.
TLR-9	Communications	The mission shall perform uplinks and downlinks through the Deep Space Network (DSN)'s 34m radio antenna.
TLR-10	Regulations	The mission shall follow the regulations encompassed by past Calls for Proposals from NASA.
TLR-11	Planetary Protection	The mission satellites' orbits shall not decay past an altitude of 150 km within 50 years from time of constellation deployment.

4.4.2 Mission Architecture & Concept of Operations

4.4.2.1 Mission Planning

We anticipate MARiO ride-along a larger mission with an estimated launch date of 2029. With that in mind, we have developed the following timeline:

Pre-Phase A (9 months): In the first 2 months, the Proposal shall be submitted containing a concept definition. In the next 3 months, the requirements definition shall be completed and in the last 4 months, the baseline of the mission architecture design baseline shall be completed.

Phase A (15 months): The first 3 months shall be dedicated to formalizing the mission architecture. Subsequently, 2 months for formalizing the requirements flow down, 3 months for the preliminary design solution, 2 months for integration, interface, and testing plans, and 5 months for technology development.

Phase B (12 months): In the first 2 months, the integration, interface and testing plans shall be completed. The next 3 months are dedicated to formalizing the design solution, then 2 months for baseline operations, decommissioning and disposal plans, and finally 5 months for technology development completion.

Phase C (14 months): An estimated 3 months are dedicated toward the final design solution definition, 4 months for COTS parts and materials order, 3 months for the satellites frame fabrication, and 4 months for software development.

Phase D (22 months): The first 3 months are dedicated to subsystem assembly. Subsequently, 3 months to satellite frame fabrication, 2 months to system integration and assembly, 4 months for

testing, 2 months for delivery and integration with the primary mission, 6 months for NASA full system testing, and 2 months for launch operations and checkout.

Phase E (34 months): An estimated 8 months will be dedicated to transferring to Mars operations, 2 months for orbital insertion and preparation to Mars, and 24 months for the primary mission duration.

Phase F (2 months): Close-out operations and activities. At this point, an assessment of lengthening the potential mission timeline will be made.

A full Gantt chart containing these phases and related major activities, including major project milestones, is included in the Appendix.

4.4.2.2 Mission Development

Should the mission be selected for funding, we plan for a collaboration between the University of Michigan and NASA's Jet Propulsion Laboratory for MARiO's design, fabrication, and testing.

Primary development will be completed at the Michigan Exploration Laboratory (MXL), which has previously developed other CubeSat missions in partnership with JPL, such as GRIFEX (https://www.jpl.nasa.gov, n.d.-a) and MCubed (https://www.jpl.nasa.gov, n.d.-b). MXL has also developed a number of independent projects, including the nanosatellite mission RAX (Cutler & Bahcivan, 2014) through the National Science Foundation.

Primary development and engineering team members will be university undergraduate and graduate students; this is a prime opportunity to strengthen an academic partnership and

create an educational opportunity for supporting and training future engineers in the aerospace industry. Systems engineering, satellite and subsystem development, COTS procurement, as well as initial testing and simulations shall be conducted by MXL members using proprietary equipment of MXL and the University of Michigan's Aerospace Engineering Department and Climate and Space Science Engineering Department, such as their thermal chamber and zero-Gauss copper chamber, shall be used for this stage of testing. Requirements may be demonstrated using simulations, such as STK orbital analysis and SPENVIS radiation analysis.

The MXL systems engineering team shall be provided with more details about specific testing guidelines or requirements provided by JPL and other NASA entities (including Mission Control) upon mission selection. During the satellite development and initial stages of testing, these shall be conducted through MXL prior to delivery to JPL. Further rigorous testing shall be conducted at JPL by systems engineers upon satellite hand-off from the MXL/University of Michigan team. These may include more rigorous thermal and vibrational tests, and other verification to ensure flight readiness.

4.4.2.3 Spacecraft Operations

NASA and JPL will oversee launch activities, which we do not detail here, since it is a ride-along mission. The CubeSats shall be contained within the selected payload carrier, detailed further in the following section. Both MXL and JPL, are jointly responsible for monitoring all the science operations, while NASA conducts all the command and real-time control operations for the spacecraft. All communications and command control from ground system to the spacecraft and vice-versa will occur through the Deep Space Network (DSN), as detailed later in the discussion of our communications architecture.

As the 6U form factor of our CubeSats does not allow for a sufficient propulsion system to perform orbital capture themselves around Mars, we necessitate the usage of an intermediary stage to enable delivery of the satellites into their orbits. We are considering a 'payload carrier' option which would in itself constitute the payload of the launch vehicle, and would be ejected from the launch vehicle towards Mars. The payload carrier has enough propulsion capability to perform orbital insertion to the altitude of the first CubeSat, dispense the satellite into its orbit, and lower to the second altitude to dispense the second satellite. This payload carrier, if it is able to remain operational for the mission duration, could also act as an additional data relay, as outlined in Section 5 of this paper. Options we are currently considering for this payload carrier architecture include the Photon by Rocket Lab, which was designed for Mars missions, in addition to the Square Rocket by Bradford Space, and the Fervoride by Momentus.

We have outlined several modes of spacecraft operations which determine which systems are operating as well as satellite pointing priority. For all modes, the on-board computer (OBC), electric power system (EPS), and attitude determination and control system (ADCS) are operational and contribute towards the primary function of the mode. The IRIS transponder (which processes signals and communications) shall always be set to at least "receive only" mode in case of any unexpected communications from the Earth.

Science Mode: RO antennae and USO are operational to transmit and receive RO signals. The transponder is set to "receive only" mode. Pointing priority is to maximize the RO link. A minimum of one RO measurement shall be collected per Martian day (approximately 25 h). The science functionality shall therefore be available for a maximum of 30 minutes per Martian day, or around 2% of the primary mission.

Communications Mode: The transponder is set to simultaneous "send and receive" mode. Pointing priority is to maximize the communications link with the Earth. The DSN availability is currently estimated at 1 h per day. This communications functionality shall therefore be available for a maximum of 1 hour per Martian day, or around 4% of the primary mission.

Standby Mode: This mode shall constitute the majority of the satellite operational time, approximately 94%. Pointing priority is towards the Sun to maximize battery charging through the EPS system. The satellites shall be on standby for the majority of their operations due to the limited data bandwidth available for transmit back to Earth. As will be discussed in Section 5 under a discussion of alternative architectures, if an additional data relay is available, more data can be transmitted back, and the time in standby mode shall be reduced.

Stationkeeping Mode: This mode enables the satellites to maintain their orbit and perform maneuvers via thrusters as minor changes in orbit occur periodically. ADCS Sensors are operational to monitor and maintain the environment, while the thruster executes stationkeeping maneuvers. These maneuvers are expected to be infrequently required, at <1% of the satellite's operational time.

Safe Mode: This mode is engaged whenever an anomaly or error is detected. As soon as Safe Mode is engaged, the satellite immediately switches to sun-facing mode to maximize power received. All unessential functions are shut down and communications with Earth are prioritized. The satellite only exits Safe Mode once given the command from Earth.

A summary of the satellite's operational time breakdown and example day of operations are included in Table 4.2 and Table 4.3.

Table 4.2 Usage of different subsystems/components during Primary Mission.

Subsystem/Component	% Usage during Primary Mission
Receive signals (IRIS)	92
Simultaneous transmit/receive signals (IRIS)	8
Comms antenna	100
RO antenna	4
Thrusters	Variable
ADCS sensors	100
OBC	100

Table 4.3 Example of modes scheduling within one Martian day.

Duration	~8 hours	30 mins	30 mins	~8 hours	30 mins	10 mins	~8 hours
Mode	Standby	Science	Comms	Standby	Comms	Station-keeping	Standby

4.4.3 Payload Operations

MARiO will determine Mars temperature, pressure, and density neutral atmospheric and ionospheric profiles by performing radio occultation. As previously described, RO is a remote sensing technique that measures the bending angles from the Doppler effect on radio frequency signals propagating through the atmosphere. An overview of this operation is depicted in *Figure 4.3*.

MARiO will perform RO observations using an Ultra Stable Oscillator (USO) as a frequency reference and the dual-frequency one-way link method. This method allows multiple RO experiments, clock error removal from the measurements, and ionospheric errors removal from the neutral atmospheric measurements. UHF and X-Band signals will provide ionospheric and neutral atmospheric measurements respectively and were chosen based on Martian heritage missions. For the spacecraft link distance and system temperature typical values of 4000 km and 300 K respectively, the average required gain is approximately 3 dB for UHF and 16 dB for X-Band frequencies. The USO shall provide time measurements for RO to a precision of 10^{-12} at 1 second.

MARiO will utilize two RO antennas as part of the architecture to transmit UHF and X-Band Signals independently, and simultaneously during an RO link. A trade study was conducted to choose the most suitable RO UHF and X- Band antennas for the design, the selections of which are detailed in the following section. An overview of this operation is depicted in Figure 4.4. The vertical resolution of the atmospheric profile derived from the measurements is influenced by the velocity at the vertical tangent point of the RO crosslink, as will be further discussed in the orbital configuration analysis.

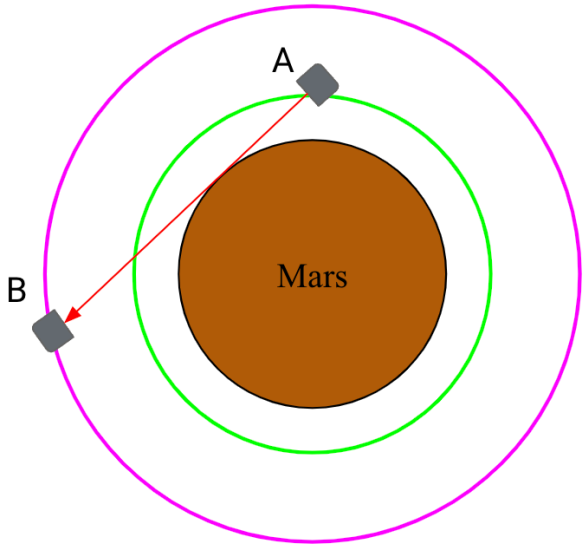

Figure 4.3 MARiO RO schematic illustration of satellites link from a planetary perspective. The vertical resolution of the derived atmospheric profile is dependent on the velocity at the tangent point.

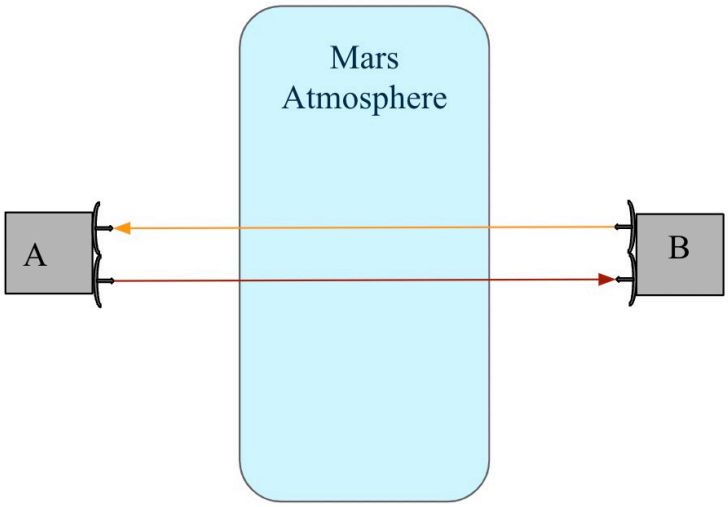

Figure 4.4 MARiO RO schematic illustration of the dual-frequency one way RO link. Both frequencies are transmitted and received simultaneously.

The MEDS instrument shall take in as input the unmodulated signals from the UHF and X-Band RO antennae. It will calculate the power and kurtosis spectra from these signals, and in

conjunction with the on-board computer, it will clean the data and search for characteristic ESD events. If any are found, these candidate events will be transmitted as data back to Earth. We have chosen to limit our transmissions only to candidate events as to reduce the overall data needed to transmit.

4.4.4 Orbital Design

It was determined from prior NASA SIMPLEx (Small Innovative Missions for PLanetary Exploration) selected missions (such as JANUS (Scheeres et al., 2020) and EscaPADE (R. Lillis et al., 2022)) that limiting the number of satellites to two was most feasible for selection as a ride along mission, and this was imposed as a constraint on the orbit selection. Further discussion of opportunities with additional satellites are discussed in section 5. In addition to the number of satellites, their specific orbital configuration is one of the most influential system drivers associated with the mission, as orbital configuration drives the amount and quality of RO opportunities for the scientific payload.

Analysis of the MEPAG scientific goals led to the selection of 10% as the minimum acceptable planetary coverage within one Martian sol. This value is To Be Reviewed (TBR) as we continue to understand and optimize the planetary coverage. However, in general, to achieve this level of performance and vertical resolution, it was found that the RO crosslink tangent point velocity must be kept within 2 km/s. In order to fulfill the top-level requirement for atmospheric measurements to capture seasonal and diurnal variability, the constellation design therefore needs to allow for each measurement region to be revisited at least 8 times per Martian year. The orbits are also required to not decay for at least 50 years, in accordance with NASA planetary protection regulations (Rummel et al., 2002) measure revisit by dividing the Martian surface into

15 x 15 degree grids, which we determined by evaluating the typical scale of climate models (Werndl, 2016).

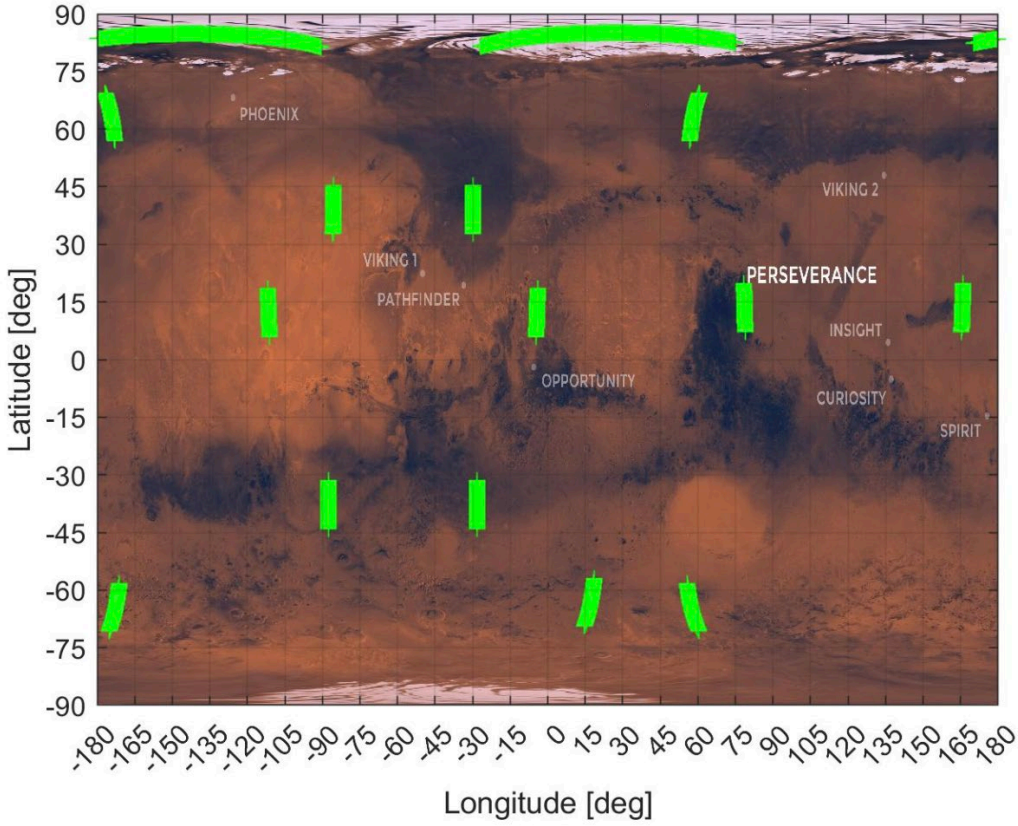

Figure 4.5 Example day of RO opportunities over the Martian surface.

Figure 4.5 depicts an example Martian day of potential RO opportunities – points where the two satellites are in view of one another and have an RO tangent point at < 2 km/s.

Due to the J2 perturbations, the inner and outer satellite precess at different rates, resulting in a range of global coverage rates throughout the Martian sol. ΔRAAN (Right Angle of Ascending Node) is a measure of the angle between the orbital planes of the satellites. Figure 4.6 depicts orbital coverage as a function of the satellites' ΔRAAN, through the range throughout one sol of 0º to 180 º. For the baseline 2-satellite configuration, the global coverage can range

between 6.9% at a 90º ΔRAAN to a maximum of 41.67% at a 120º ΔRAAN, for a yearly average of 12.13% global coverage.

The current orbital configuration, selected to maximize global coverage for RO opportunities, is as follows: The 'outer' CubeSat has an altitude of 2500 km, with an inclination of 85º and an eccentricity of 0º. The 'inner' CubeSat has an altitude of 500 km, the same inclination and eccentricity. To comply with planetary protection regulations on the timeline of de-orbit, 400 km was set as a minimum altitude when performing this analysis.

Substantial analysis was performed to optimize the orbital configuration. We utilized a MATLAB script, running an STK simulation which calculates the number of radio occultation opportunities. We seek to maximize this number by varying the six orbital elements for the cases of 2, 3, and 4 satellites. The STK simulation can be considered a black-box, and therefore we eliminate any standard gradient-based optimizations which require a supplied external function. The global optimum is of interest, not just a local one, though there is value in the optimizer returning a few options for optimal local coverage. We ideally also want to use MATLAB for optimization to bypass any compatibility issues. For this reason, the initial suggestion is to use the non-gradient optimizers in MATLAB's Global Optimization Toolbox. Thus far, pattern search has been our primary optimization methodology due to its fast convergence and ability to handle all types of constraints. Genetic algorithms and other options are also being considered in case of failure for pattern search. To attempt optimization, these algorithms only need to be fed initial values or simulations results which can be gained from trial runs.

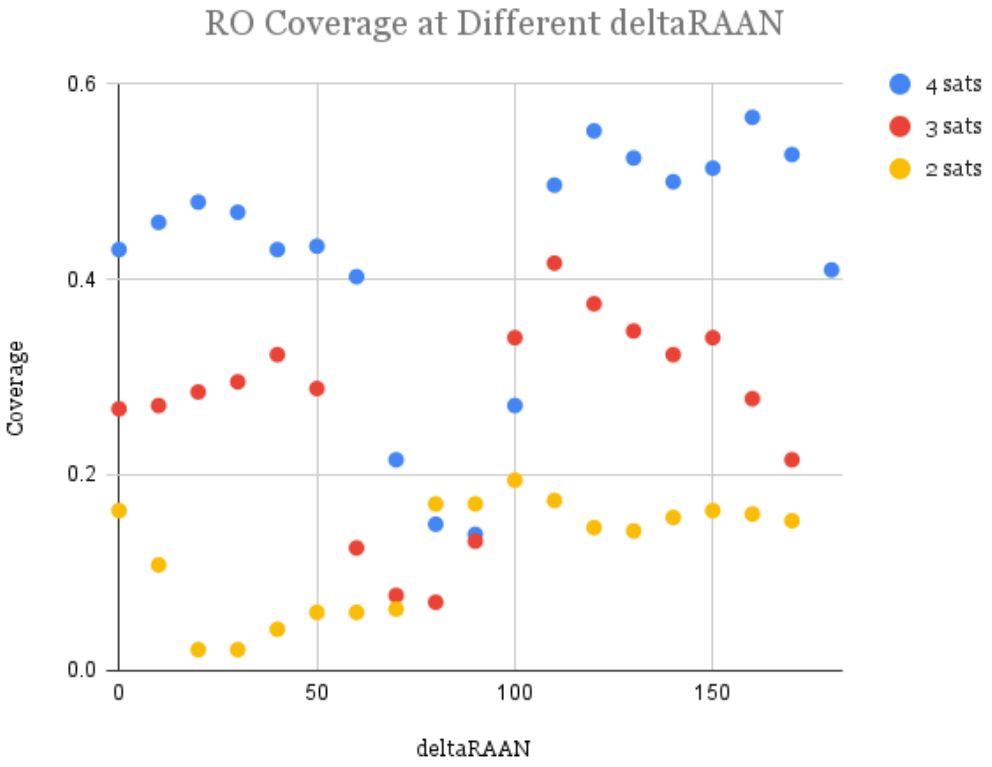

Figure 4.6 Global coverage comparisons for considered CubeSat architectures as a function of the ΔRAAN, which changes throughout the year.

4.4.5 CubeSat Design

For each major subsystem, comprehensive trade studies were conducted to identify and select appropriate COTS (commercial-off-the-shelf) components for the CubeSat design. COTS parts were utilized when possible, to reduce mission cost, development complexity, and maintain higher TRL (Technology Readiness Level).

For the RO payload system, two antennae and a USO (Ultra-Stable Oscillator) were selected. MARiO will use a 9700 Ultra Miniature Space-Qualified OCXO from Microship, which meets the Allan deviation requirements for precision. The RO antennae shall be the UHF 437Hz QHA Antenna from Helical Communications and the X-Band 4x4 Path Array Antenna

from Endurosat, as selected through a trade study. The X-Band Antennae operates at a frequency of 8025-8400 MHz with a gain of 16 dBi.

The propulsion system shall be the Busek BET-300P passive electrospray thruster. It was selected as the best fit for the MARiO cubesats' form factor for its low mass and notably higher thrust-to-power ratio/specific impulse when compared to other thruster types. This thruster, built by BUSEK Space Propulsion and Systems, is a self-contained unit consisting of a passively-fed electrospray thruster, a Carbon Nanotube Field Emission Cathode, and supporting electronic control module. The total system has a mass of about a kilogram, delivers a specific impulse of roughly 2300s, and with 100g of propellant is capable of delivering approximately 113 m/s of ΔV.

For the system overseeing communications to Earth, the Iris transponder developed by JPL shall be utilized (Duncan et al., n.d.). Other COTS options surveyed were incapable of handling the frequency required of Earth-to-sat communications, as our selected frequency range is 32 to 34 GHz in the Ka-band. In addition to this transponder, the Ka-band antenna from Optisys was selected as the communications antenna, with a gain of 36.2 dB. Another option, the KaPDA (in-house antenna from NASA) had improved performance, but was determined to be too large to fit on the 6U structure. Both CubeSats have their own independent communication capability back to Earth. This allows for simultaneous data transmission from both satellites to maximize the data received during DSN windows, as well as to increase redundancy. Both the science data and telemetry and housekeeping data need to be encoded before they can be transmitted back to Earth. Per recommendations by the DSN and conforming to CCSDS standards, the MARiO mission shall use turbo encoding.

Attitude determination & control (ADCS) is a very important part of the system, as the pointing of the satellites are critical to performing precise RO links with the opposing satellite. To achieve our scientific and mission goals, it was determined that ADCS system shall deliver at least 14 mN-m of torque on each axis, a slew rate of 2.4 degrees per second, and shall store 0.512 mN-m-s of momentum on each axis. For pointing accuracy requirements, the system shall achieve a maximum accuracy of 0.14 degrees for DSN link, and 3.7 degrees for RO measurements. To achieve these requirements, the Standard NST star tracker from Blue Canyon Technologies, the NFSS-411 sun sensor by NewSpace, the NavChip IMU from Intersense, and the RL-RW-0.06 reaction wheels by Rocketlab were selected. The system shall have 4 reaction wheels and 1 of each of the other components.

For the command & data handling (CDH) system, the on-board computer (OBC) was selected based on RO data rate and housekeeping data rate estimates. Further information on the estimated RO data rates are provided in Tables Table 4.4 and Table 4.5. These values are based on the assumption that the DSN will allow approximately 1 hour access per day for low priority missions (30 minutes passes for each satellite), with up to 4 simultaneous downlinks. This was utilized as a guideline for our mission design after talks with DSN personnel.

The selected OBC is the NanoAvionics SatBus 3C2, which has a processing speed of 200 MHz speed configurable up to 400 MHz. For storage, micro SD cards shall be used, which can hold up to 1 TB of data. The selected OBC has 20 kRad of radiation hardening, which was determined to be sufficiently protected for the mission environment. It also encases the SD card, so this component will be protected as well. For use with the OBC, F Prime was selected as the software language (Bocchino et al., n.d.).

Table 4.4 Data Generation Rates.

Source	Raw Data	Encoded Data
Housekeeping	0.988 MB/Day	1.99 MB/Day
RO	1.00 MB/RO	2.02 MB/RO

Table 4.5 Data Budget.

Earth-Mars Distance	Max Data-Rate [kbps]	Max Transmittable Data Per Sat [MB]	Max Ros Per Sat Per Day	Total Max Ros Per Day
Furthest	2.82	1.24	0	0
Average	14.8	6.50	2.23	4.46
Closest	151	66.5	30.0	60.0

Thermal analysis was conducted based on the orbital altitudes of both satellites primarily based on techniques from SMAD: Space mission and design analysis (Gilmore, 1994; Wertz et al., 2011). Our batteries selection defined the thermal requirements for the satellites, with an operational minimum and maximum of 0º to 40 º C, and a survival minimum and maximum of -10º to 50º C. Due to their differing environments, the inner and outer satellites have different thermal requirements. The inner satellite requires a radiating surface of dimensions 0.0133 m^2, which is satisfied with the use of MLI covering the external surface besides the antennae, engine exhaust, and solar panels. The MLI chosen was DUNMORE MO20294: STAMET / 275 GA DuPontTM Black Kapton® XC Polyimide Film. The Black Kapton layer provides the aforementioned electric resistivity and the Stamet layer provides radiation protection. The outer satellite requires a heater to provide 4.6 W of heat to the satellite's internal components, to be

placed close to the batteries and X-band antenna on the structure. A 1”x1” patch of Omega Kapton® Insulated Flexible Heaters shall provide the required heating.

Based on the selected components, an electrical power budget was calculated for each CubeSat, presented in Table 4.6.

Table 4.6 EPS Budget.

Subsystems	Power	Operational Time as % of Orbit Time
Transmit Only	30.8 W	0%
Receive Only	12.6 W	92%
Simultaneous Tx/Rx	35.0 W	8%
ADCS Sensors	1.5 W	100%
Wheels	2.7 W	3%
CDH	6.4 W	100%
Propulsion	16.5 W	Variable
Required (30% Margin)	**32.6 W (+4.6 W of heater for outer)**	

Based on the required power of 32.6 W for the inner satellite, and 37.2 W for the outer satellite, solar panels were selected for use. The best option was the MMA Design HaWK 17AB36 - hvHaWK solar panels. MMA Design was also the supplier of EPS parts used in the 2018 MarCO mission, a similar CubeSat mission to Mars (Schoolcraft et al., 2016). The solar arrays were chosen in the high voltage configuration, deployment axis α+SADA(β). The motor that orients the arrays, Solar Array Drive Assembly (SADA), chosen was the MOOG Type 1. Further analysis using the SPENVIS simulation software yields a required solar panel coverglass thickness of 70 micrometers for the Martian environment.

In addition to the power supply requirement, EPS shall provide nominal power whilst not charging. This results in the orbit selection significantly influencing battery requirements, where the battery must be capable of fully charging between eclipses. Eclipse analysis of the baseline architecture's orbital configuration yields a minimum battery capacity of 42.0 W-hrs, leading to the selection of the EaglePitcher Technologies 13 Ah Lithium-Ion Pouch Cell as our batteries. Two batteries shall be utilized.

The CubeSats were early on determined to be 6U to demonstrate the feasibility of a compact planetary science mission. The extended assembly for the final design is depicted in Figure 4.7. This form factor was taken as a baseline for the rest of the structural design and integration of the selected components. We intend to fabricate the CubeSat frames in-house with Aluminum–7075, one of the strongest aluminum alloys available that is also 3D-printable. The frame shall have dimensions of 11.2 cm x 20.03 cm x 30.54 cm and an estimated mass of 592 grams.

Figure 4.7 MARiO CubeSat; the helical UHF antenna and solar panels are extended in their operational assembly.

Figure 4.8 depicts the arrangement of components within the interior of the satellite. Parts were arranged as to disperse weight as evenly as possible throughout the satellite, which is crucial for thruster and sensor functionality. A center of mass analysis performed through SolidWorks indicates a center-of-mass near exactly on the geometric central axes of the satellite, with less than a centimeter of difference. This can be further refined when other components, such as wires, screws, and bolts, are taken into account. An overview of all components is included in Table 4.7. Our overall CubeSat mass comes to 10.0 kg, which can be compared with our closest mission analog, MarCO, which weighed 13.5 kg per satellite.

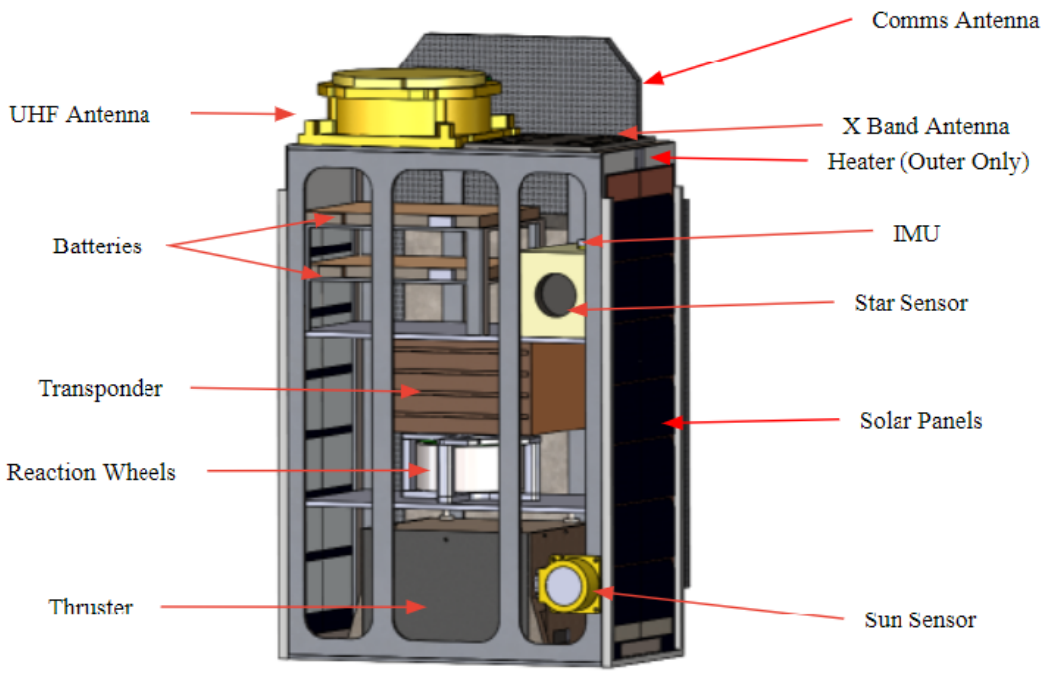

Figure 4.8 MARiO CubeSat; interior components labelled. The solar panels and helical UHF antenna are in their stowed assembly.

Table 4.7 Mass and volume analysis by MARiO subsystem.

Subsystem	Mass	Volume
Payload/RO	1.30 kg	1039 cm^3
ADCS	0.94 kg	1065 cm^3
CDH	0.27 kg	280 cm^3
Structures	0.59 kg	N/A
Comms	1.70 kg	(Exterior)
Propulsion (wet)	1.10 kg	1052 cm^3
EPS	4.10 kg	418 cm^3
Thermal	42 g (Outer) 75 g (Inner)	(Exterior)
Total	**10.0 kg**	**6U Form Factor: 6207 cm^3** **Interior Components Volume: 3854 cm^3**

4.5 Project Management & Paths Forward

Risk analysis was conducted for all subsystems and for the mission as a whole. While the entire analysis will not be presented here, an overview of the analysis and mitigation efforts is depicted in Figure 4.9 and Figure 4.10. Out of the 65 risks identified across the mission design, 30 were classified as needing mitigation, while 27 were classified as to be watched, and 8 were accepted. After mitigation strategies were implemented, all 'red' risks were eliminated, while the number of risks in the 'yellow' (to be watched) classification was significantly reduced. 7 risks from astrodynamics, 3 from propulsion, 7 from structures, 8 from ADCS, 3 from communications, and from C&DH were mitigated.

Initial project management work was completed for systems engineering planning purposes. Costs were compiled for all selected COTS parts, and labor estimates were provided

on the assumption of majority workforce comprised of university students. With current estimates, the mission currently comes in at $18.35M after margin and reserve implementation. As a comparison, our closest mission analogy, the MarCO CubeSat mission, cost around $18.5M. This cost currently does not include development and fabrication of the ESD spectrometer device, for which we are still working to understand the technical cost and potential schedule.

For a planned ride-along mission launching in 2029, a project schedule was created detailing development stages and planned review timelines for the mission. Delays were implemented for review feedback and implementation prior to resuming work. The full schedule is detailed in Appendix Figure A.1. We intend to propose this mission, after review and implementing feedback from the academic community, for the next round of NASA SIMPLEx calls for proposals.

The mission architecture of 2 CubeSats presented in this paper is the minimum viable architecture to achieve radio occultation measurements. Given additional funding opportunities and a larger launch volume allocation, additional numbers of CubeSats can significantly increase the number of RO opportunities, collected scientific data, and data transmissions back to Earth. Since the DSN can accommodate up to 4 downlinks at once, we have limited our alternate architecture analysis to a maximum of 4 satellites.

In Figure 4.6, comparisons in global coverage have been made between our current 2-satellite architecture and potential 3-satellite and 4-satellite architectures. For 3 satellites, we achieve an average global coverage of 26.48%, with a minimum of 12.5% and a maximum of 41.67%. For 4 satellites, we achieve an average global coverage of 41.94%, with a minimum of 13.89% and a maximum of 56.60%.

With additional satellites, our mission budget will increase for both the actual satellite cost and labor cost. For 3 satellites, we anticipate our satellite and labor costs will increase by 50%, leading to total allocations of $5.07M and $8.4M respectively, and bringing up the total mission allocation to $22.72M. For 4 satellites, the satellite and labor costs increase respectively to $6.76M and $11.2M, and leading to a total mission allocation of $27.21M.

In addition to an increase in opportunities to collect RO data, we also must consider that for 3 satellites, an extra 50% more scientific data will be able to be transmitted back to Earth, and for 4 satellites, this increases to 100% due to the extra communications links. Extra development budget might also allow us to create an additional communications link through the payload carrier itself, utilizing it as a data relay opportunity. This would be most suited to 2 and 3 satellite configurations, since the DSN allows for up to 4 simultaneous downlinks.

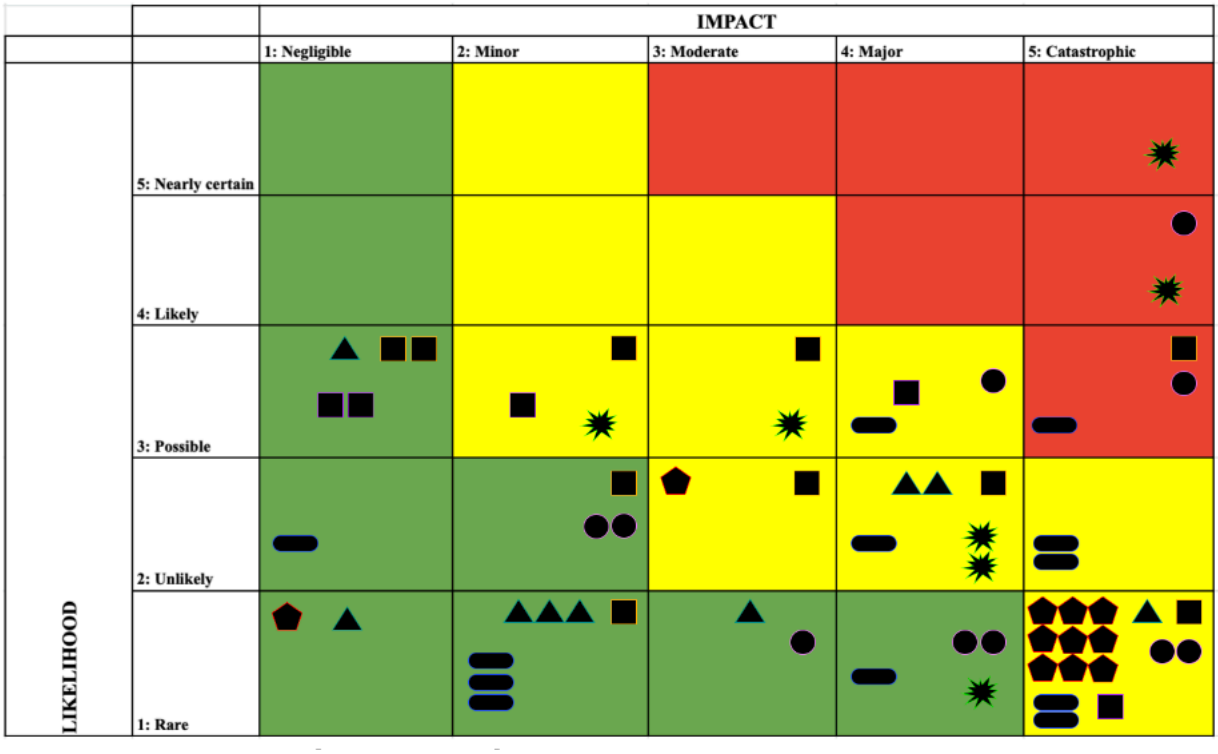

Figure 4.9 Risk analysis pre-mitigation strategy implementation. Risks were identified for astrodynamics, propulsion, communications, ADCS, C\&DH, structures, and thermal/EPS subsystems.

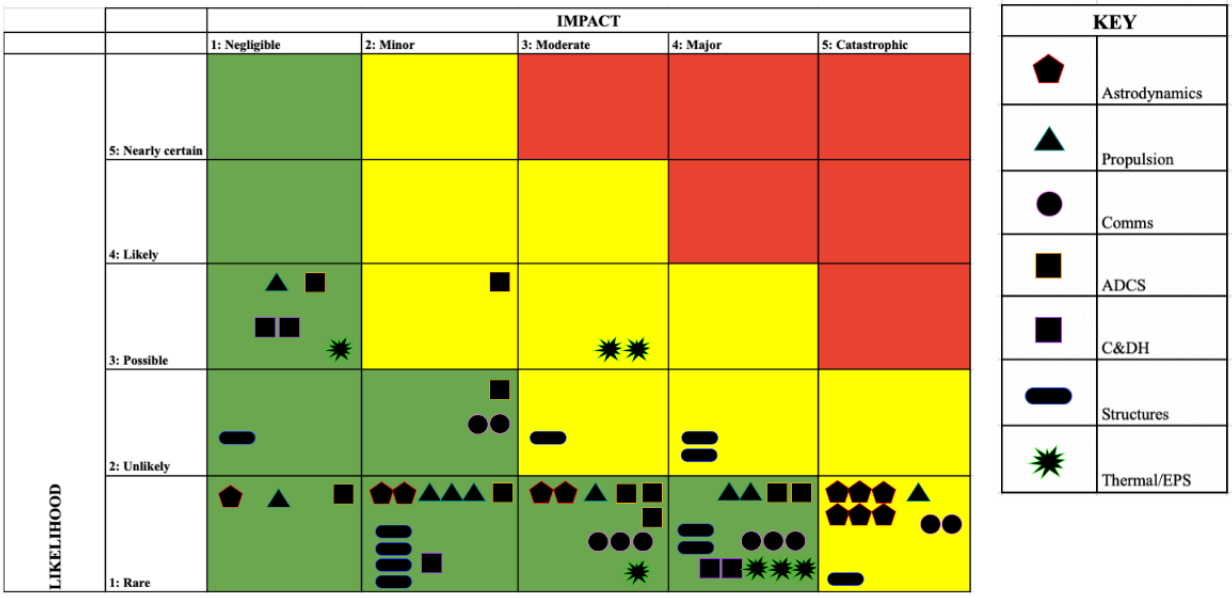

Figure 4.10 Risk analysis post mitigation strategy implementation. High (red) risks are eliminated, and medium (yellow) risks are substantially reduced.

4.6 Summary & Conclusions

We present a low cost, CubeSat mission for Mars to perform dedicated RO measurements over the course of one Mars year. The motivation behind such a mission is driven by MEPAG science goals, mainly to prepare for human exploration of the surface and to understand the past and present climate of Mars. By using RO data at different local solar times and seasonally, engineering models can be properly calibrated in preparation for EDL operations. The large electrostatic potential also presents an unknown risk to humans and electronics on the surface. As a secondary science objective, we aim to use RO signals to detect and locate sources of ESD from the surface of Mars. A dual frequency one-way method will allow for a more compact USO that will fit on board a 6U spacecraft, but will still achieve the same accuracy and precision as past RO experiments. The MARiO mission is driven by the aforementioned science objectives and all system and sub-system requirements presented are derived accordingly. In our satellite designs, we have sought lower-cost COTS without required development costs for individual components. We have sought to present a concept of operations architecture limited to 2 satellites for a realistic mission concept which might be selected for funding.

Chapter 5

Summary and Conclusions

EDL is the most challenging and high-risk phase of any surface mission. Knowledge gaps in models used for predicting atmospheric conditions at targeted landing sites currently limits their application. A dedicated fleet of SmallSats offer a cost-effective solution to gather enough data to initialize these models and better predict conditions for autonomous and human crewed spacecraft on the surface of Mars. Given the recent interest in SmallSat technology, more COTS parts are available for new missions and pathfinder missions such as MarCO have paved the way for interplanetary SmallSat capabilities.

With the latest MEPAG report and support of science and engineering teams at JPL, we have developed a list of top-level requirements to mature a mission concept primarily objective as RO experiments with secondary objective as ESD detection. Our analysis shows that by implementing DOW frequency observations to measure the phase, a smaller and cheaper COTS USO can be used to achieve the same accuracy results as past RO missions, which used a higher stable USO on board.

The first iteration of our mission concept relied on a Monte Carlo simulation code which artificially introduced thermal and clock noise into truth bending angle profiles to characterize

pressure, temperature and number density uncertainties. Two different frequencies are used to separate ionosphere electron densities from neutral atmosphere components. In addition to using real RO profile data, the code can also implement synthetic exponential neutral atmosphere pressure based on the ideal gas law for CO_2 and hydrostatic balance. The ionosphere is also modelled using a Chapman model that is dependent on the local SZA (Solar Zenith Angle).

The code relied on a simple white noise method to approximate the clock noise, however a more rigorous approach to clock noise was introduced in Chapter 3. The analysis from Chapter 2 shows that a traditional size USO would be needed, which is an unrealistic expectation to fit inside of a 6U SmallSat.

A method of modelling clock noise more precisely was introduced into the Monte Carlo simulation code. This was accomplished through adding noise in the frequency domain within the range of frequencies that correspond to integration times of typical RO measurements. Analysis shows that the expected clock error was on the same order of magnitude of the white noise method. Chapter 3 also introduced the DOW frequency method typically used in gravity ranging experiments. This self-cancelling algorithm was implemented into the simulation code and analysis shows a smaller and less stable clock can achieve the required 1K temperature uncertainty required for the mission.

Finally, the full mission architecture which offers detailed systems engineering analysis is included as Chapter 4. Designed as a NASA SIMPLEx type mission, the use of a fleet of SmallSats to accomplish top level science requirements is a low-cost solution to offer unprecedented coverage of Mars in support of EDL. This chapter outlines an orbital analysis for optimal configuration at high inclinations to maximize the latitudinal coverage. The systems

engineering addresses all systems and sub-systems, including communications, power, payload, structures, ADCS and propulsion. Some flexibility to change aspects of the mission depending on the call for proposal are shown in the form of trade studies, which show options for 2, 3 or 4 SmallSats in the configuration. With feedback from teams at JPL, we hope this work will provide a basis for a successful future mission to support EDL operations and human exploration on the surface of Mars.

Appendix

A.1 Supplementary Material for Chapter II

A.1.1 Clock Noise

Consider carrier frequency *f* (and corresponding wavelength λ) and sampling time Δt between successive phase measurements. From one sample to the next, the error in the phase (in units of length) due to clock instability is

$$\Delta\phi_c = c(b_t + b_r) \tag{A1}$$

where c is the speed of light, b_t is the clock drift from the transmitter in time Δt, b_r is the clock drift from the receiver in time Δt. Modeling the clock noise as a random uncorrelated white noise, the standard deviation of the clock noise on the phase can be estimated as

$$\sigma_c = \sqrt{\sigma_t^2 + \sigma_r^2} \tag{A2}$$

If the transmitter and receiver have the same kind of oscillator, then $\sigma_t = \sigma_r$ and $\sigma_c = 2\sigma_r$. Given AD over Δt,

$$\sigma_r = c(AD \times \Delta t) \tag{A3}$$

The Doppler shift is the time derivative of the phase. Thus, the Doppler shift error (in Hz) can be estimated as

$$\sigma_{clock} = \frac{\sqrt{2}}{\lambda \Delta t} \sigma_c \quad (A4)$$

For example, if Δt = 1s and AD = 1 x 10^{-12} s/s, then σ_r = 0.3 mm. For an X-band occultation, λ = 8.4 mHz, and σ_{clock} = 8.4 mHz, the bending angle error can be calculated from the frequency error as

$$\sigma_\alpha = \frac{\lambda}{v_{tpz}} \sigma_{clock} \quad (A5)$$

Where v_{tpz} is the vertical velocity of the ray tangent point. Continuing the example above, for v_{tpz} = 1 km/s, σ_α = 0.3 μrad.

A.1.2 Thermal Noise

$$\sigma_{\text{thermal}} = \frac{\sqrt{2BN_0/C}}{2\pi\tau_{\text{thermal}}} \quad (A6)$$

Where C/N_0 is SNR in dB Hz, C is the power in W, N_0 is the noise power density in W Hz^{-1}, 2B is the noise bandwidth in Hz, and $\tau_{thermal}$ is the time interval of the measurement in s.

A.1.3 Neutral Atmosphere Profiles

$$N = N_0 e^{-z/H} \quad (A7)$$

Where z is the height in km and H is the scale height at Mars of 10 km. N_0 has expected value of 3.82 N-units (Ao et al., 2015).

A.1.4 Abelian Transforms

$$\alpha(a) = -2a \int_a^\infty \frac{1}{\sqrt{a'^2 - a^2}} \frac{\mathrm{d}\ln(n)}{\mathrm{d}a'} \mathrm{d}a' \quad (A8)$$

$$\ln\big(n(a)\big) = \frac{1}{\pi}\int_{a}^{\infty} \frac{\alpha(a')}{\sqrt{a'^2 - a^2}}\,\mathrm{d}a' \qquad (A9)$$

The forward Abel transform converts refractive index to bending angle (equation A8), and the inverse transform converts bending angle to refractive index (equation A9). In both equations a is the impact parameter defined as the refractive index times the radius of curvature or a = r x n. The upper limit of the integral is the atmosphere edge, ~200 km in our simulations.

To avoid singularities in both integrals of equations A8 and A9, a change of variables is done. Substituting in for the impact parameter, a = x sin(θ) and evaluating the integrals from the lower limit of $\sin^{-1}(a/a_t)$, where a_t is the impact parameter at the top of the atmosphere, to the maximum of the function at π/2.

A.1 Supplementary Material for Chapter III

The simulation solves for the coefficients given the ADs at each specified time scale using matrix multiplication. Using the notation from equation 2, each h_n coefficient is defined as

$$\begin{bmatrix} A_{2,1} & A_{2,2} & A_{2,3} \\ A_{3,1} & A_{3,2} & A_{3,3} \\ A_{4,1} & A_{4,2} & A_{4,3} \end{bmatrix} \begin{bmatrix} h_2 \\ h_3 \\ h_4 \end{bmatrix} = \begin{bmatrix} \sigma_2^2 \\ \sigma_3^2 \\ \sigma_4^2 \end{bmatrix}$$

In this case, the 3x3 A terms are each term on the right side of equation 3 without the h coefficients. The second 3x1 matrix is the separated unknown coefficients. Finally, the last 3x1 matrix are the ADs at different integration times. We can solve for the h_n coefficients by taking the inverse of the 3x3 matrix and dotting it with the 3x1 AD matrix as

$$\begin{bmatrix} h_2 \\ h_3 \\ h_4 \end{bmatrix} = \begin{bmatrix} A_{2,1} & A_{2,2} & A_{2,3} \\ A_{3,1} & A_{3,2} & A_{3,3} \\ A_{4,1} & A_{4,2} & A_{4,3} \end{bmatrix}^{-1} \cdot \begin{bmatrix} \sigma_2^2 \\ \sigma_3^2 \\ \sigma_4^2 \end{bmatrix}$$

A.1 Supplementary Material for Chapter IV

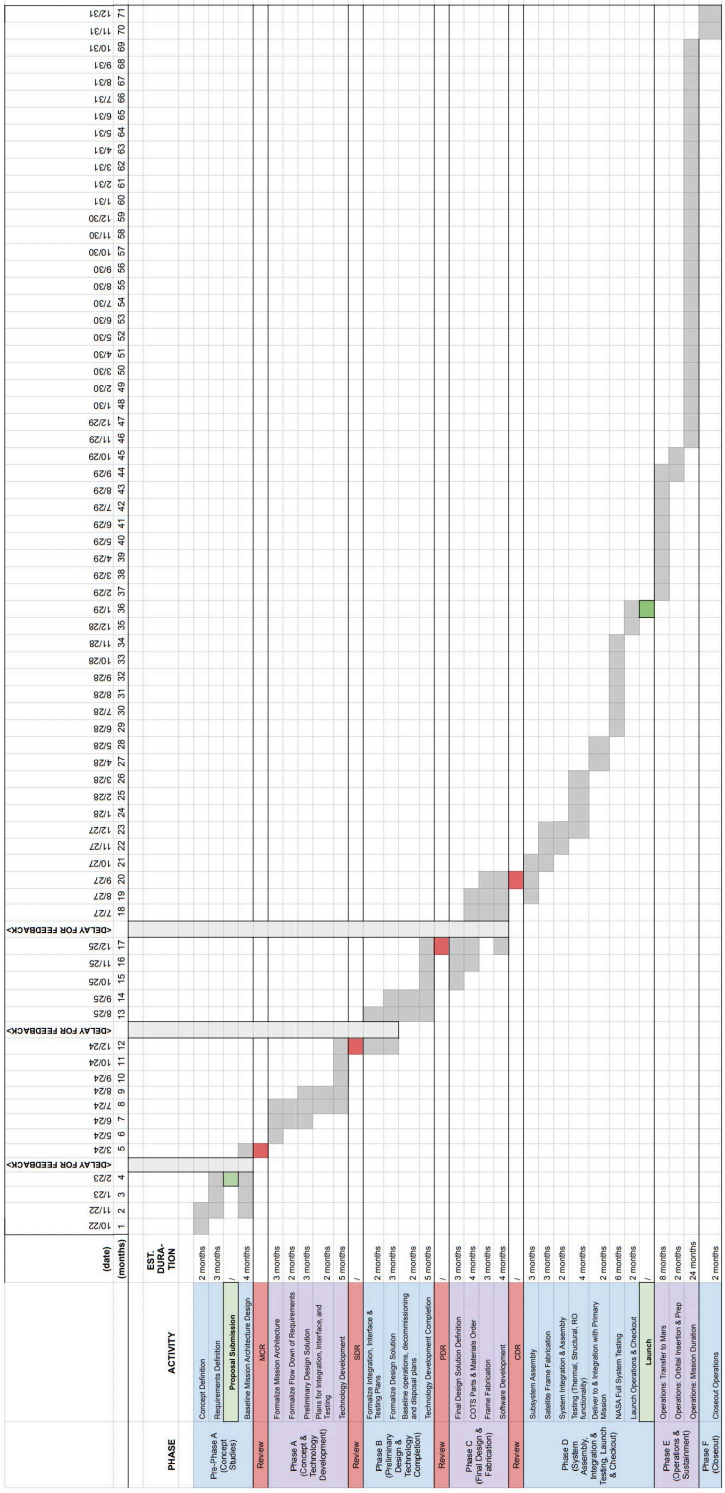

Figure A.1. MARiO estimated project schedule

Bibliography

Anderson, M. M., Siemion, A. P. V., Barott, W. C., Bower, G. C., Delory, G. T., de Pater, I., & Werthimer, D. (2012). THE ALLEN TELESCOPE ARRAY SEARCH FOR ELECTROSTATIC DISCHARGES ON MARS. *The Astrophysical Journal*, *744*(1), 15. https://doi.org/10.1088/0004-637X/744/1/15

Ao, C. O., Edwards, C. D., Kahan, D. S., Pi, X., Asmar, S. W., & Mannucci, A. J. (2015). A first demonstration of Mars crosslink occultation measurements: MARS CROSSLINK OCCULTATION. *Radio Science*, *50*(10), 997–1007. https://doi.org/10.1002/2015RS005750

Banfield, D. (2020). MEPAG (2020), Mars Scientific Goals, Objectives, Investigations, and Priorities. *White Paper Posted March, 2020 by the Mars Exploration Program Analysis Group (MEPAG) at Https://Mepag.Jpl.Nasa.Gov/Reports.Cfm.*, 89.

Barnes, J. A., Chi, A. R., Cutler, L. S., Healey, D. J., Leeson, D. B., McGunigal, T. E., Mullen, J. A., Smith, W. L., Sydnor, R. L., Vessot, R. F. C., & Winkler, G. M. R. (1971). Characterization of Frequency Stability. *IEEE Transactions on Instrumentation and Measurement*, *IM–20*(2), 105–120. https://doi.org/10.1109/TIM.1971.5570702

Bocchino, R., Canham, T., Watney, G., Reder, L., & Levison, J. (n.d.). *F Prime: An Open-Source Framework for Small-Scale Flight Software Systems*. 19.

Born, M., Wolf, E., Bhatia, A. B., Clemmow, P. C., Gabor, D., Stokes, A. R., Taylor, A. M., Wilcock. W. L, & Wayman, P. A. (1980). *Principles of optics: Electromagnetic theory of*

propagation, interference and diffraction of light. Elsevier Science. https://ebookcentral.proquest.com/lib/sfu-ebooks/detail.action?docID=4586942

Carr, M. H. (1987). Water on Mars. *Nature*, *326*(6108), 30–35.

Christensen, P. R., Bandfield, J. L., Hamilton, V. E., Ruff, S. W., Kieffer, H. H., Titus, T. N., Malin, M. C., Morris, R. V., Lane, M. D., Clark, R. L., Jakosky, B. M., Mellon, M. T., Pearl, J. C., Conrath, B. J., Smith, M. D., Clancy, R. T., Kuzmin, R. O., Roush, T., Mehall, G. L., … Greenfield, M. (2001). Mars Global Surveyor Thermal Emission Spectrometer experiment: Investigation description and surface science results. *Journal of Geophysical Research: Planets*, *106*(E10), 23823–23871. https://doi.org/10.1029/2000JE001370

Cutler, J. W., & Bahcivan, H. (2014). Radio Aurora Explorer: A Mission Overview. *Journal of Spacecraft and Rockets*, *51*(1), 39–47. https://doi.org/10.2514/1.A32436

Duncan, C. B., Smith, A. E., Aguirre, F. H., Grove, O., & Duncan, C. B. (n.d.). *Iris Transponder – Communications and Navigation for Deep Space.* 10.

Eshleman, V. R., Tyler, G. L., Wood, G. E., Lindal, G. F., Anderson, J. D., Levy, G. S., & Croft, T. A. (1979). Radio Science with Voyager 1 at Jupiter: Preliminary Profiles of the Atmosphere and Ionosphere. *Science*, *204*(4396), 976–978. https://doi.org/10.1126/science.204.4396.976

Fjeldbo, G., Eshleman, V. R., Garriott, O. K., & Smith, F. L. (1965). The two-frequency bistatic radar-occultation method for the study of planetary ionospheres. *Journal of Geophysical Research*, *70*(15), 3701–3710. https://doi.org/10.1029/JZ070i015p03701

Fjeldbo, G., Kliore, A. J., & Eshleman, V. R. (1971). The Neutral Atmosphere of Venus as Studied with the Mariner V Radio Occultation Experiments. *The Astronomical Journal*, *76*, 123. https://doi.org/10.1086/111096

Gilmore, D. G. (Ed.). (1994). *Satellite thermal control handbook*. Aerospace Corporation Press.

Golombek, M., Kass, D., Williams, N., Warner, N., Daubar, I., Piqueux, S., Charalambous, C., & Pike, W. T. (2020). Assessment of InSight Landing Site Predictions. *Journal of Geophysical Research: Planets*, *125*(8). https://doi.org/10.1029/2020JE006502

Golombek, M., Kipp, D., Warner, N., Daubar, I. J., Fergason, R., Kirk, R. L., Beyer, R., Huertas, A., Piqueux, S., Putzig, N. E., Campbell, B. A., Morgan, G. A., Charalambous, C., Pike, W. T., Gwinner, K., Calef, F., Kass, D., Mischna, M., Ashley, J., … Banerdt, W. B. (2017). Selection of the InSight Landing Site. *Space Science Reviews*, *211*(1–4), 5–95. https://doi.org/10.1007/s11214-016-0321-9

Golombek, M. P., Grant, J. A., Parker, T. J., Kass, D. M., Crisp, J. A., Squyres, S. W., Haldemann, A. F. C., Adler, M., Lee, W. J., Bridges, N. T., Arvidson, R. E., Carr, M. H., Kirk, R. L., Knocke, P. C., Roncoli, R. B., Weitz, C. M., Schofield, J. T., Zurek, R. W., Christensen, P. R., … Rice, J. W. (2003). Selection of the Mars Exploration Rover landing sites: SELECTION OF MER LANDING SITES. *Journal of Geophysical Research: Planets*, *108*(E12). https://doi.org/10.1029/2003JE002074

Hajj, G. A., Kursinski, E. R., Romans, L. J., Bertiger, W. I., & Leroy, S. S. (2002). A technical description of atmospheric sounding by GPS occultation. *Journal of Atmospheric and Solar-Terrestrial Physics*, *64*(4), 451–469. https://doi.org/10.1016/S1364-6826(01)00114-6

Harrison, R. G., Barth, E., Esposito, F., Merrison, J., Montmessin, F., Aplin, K. L., Borlina, C., Berthelier, J. J., Déprez, G., Farrell, W. M., Houghton, I. M. P., Renno, N. O., Nicoll, K. A., Tripathi, S. N., & Zimmerman, M. (2016). Applications of Electrified Dust and Dust Devil Electrodynamics to Martian Atmospheric Electricity. *Space Science Reviews*, *203*(1–4), 299–345. https://doi.org/10.1007/s11214-016-0241-8

Hinson, D. P., Asmar, S. W., Kahan, D. S., Akopian, V., Haberle, R. M., Spiga, A., Schofield, J. T., Kleinböhl, A., Abdou, W. A., Lewis, S. R., Paik, M., & Maalouf, S. G. (2014). Initial results from radio occultation measurements with the Mars Reconnaissance Orbiter: A nocturnal mixed layer in the tropics and comparisons with polar profiles from the Mars Climate Sounder. *Icarus*, *243*, 91–103. https://doi.org/10.1016/j.icarus.2014.09.019

Hinson, D. P., Simpson, R. A., Twicken, J. D., Tyler, G. L., & Flasar, F. M. (1999). Initial results from radio occultation measurements with Mars Global Surveyor. *Journal of Geophysical Research: Planets*, *104*(E11), 26997–27012. https://doi.org/10.1029/1999JE001069

Hinson, D. P., Twicken, J. D., & Karayel, E. T. (1998). Jupiter's ionosphere: New results from Voyager 2 radio occultation measurements. *Journal of Geophysical Research: Space Physics*, *103*(A5), 9505–9520. https://doi.org/10.1029/97JA03689

Ho, C., Golshan, N., & Kliore, A. (2002). *Radio Wave Propagation Handbook for Communication on and Around Mars*. 116.

https://www.jpl.nasa.gov. (n.d.-a). *GEO-CAPE ROIC In-Flight Performance Experiment (GRIFEX)*. NASA Jet Propulsion Laboratory (JPL). Retrieved October 14, 2022, from https://www.jpl.nasa.gov/missions/geo-cape-roic-in-flight-performance-experiment-grifex

https://www.jpl.nasa.gov. (n.d.-b). *M-Cubed/COVE-2*. NASA Jet Propulsion Laboratory (JPL). Retrieved October 14, 2022, from https://www.jpl.nasa.gov/missions/m-cubed-cove-2

Kass, D. M., Schofield, J. T., Kleinböhl, A., McCleese, D. J., Heavens, N. G., Shirley, J. H., & Steele, L. J. (2020). Mars Climate Sounder Observation of Mars' 2018 Global Dust Storm. *Geophysical Research Letters*, *47*(23). https://doi.org/10.1029/2019GL083931

Kass, D. M., Schofield, J. T., Michaels, T. I., Rafkin, S. C. R., Richardson, M. I., & Toigo, A. D. (2003). Analysis of atmospheric mesoscale models for entry, descent, and landing: EDL MESOSCALE ANALYSIS. *Journal of Geophysical Research: Planets*, *108*(E12). https://doi.org/10.1029/2003JE002065

Kliore, A., Cain, D. L., Levy, G. S., Eshleman, V. R., Fjeldbo, G., & Drake, F. D. (1965). Occultation experiment: Results of the first direct measurement of Mars's atmosphere and ionosphere. *Science*, *149*(3689), 1243–1248.

Kok, J. F., & Renno, N. O. (2006). Enhancement of the emission of mineral dust aerosols by electric forces. *Geophysical Research Letters*, *33*(19).

Kursinski, E. R., Hajj, G. A., Schofield, J. T., Linfield, R. P., & Hardy, K. R. (1997). Observing Earth's atmosphere with radio occultation measurements using the Global Positioning System. *Journal of Geophysical Research: Atmospheres*, *102*(D19), 23429–23465. https://doi.org/10.1029/97JD01569

Lillis, R. J., Heavens, N. G., Montabone, L., Guzewich, S., Curry, S. M., Withers, P., Chaffin, M., Harrison, T. N., Ao, C. O., Mitchell, D. L., Luhmann, J. G., Deighan, J. I., Kahre, M., Brecht, A., Neish, C., Hook, J. V., England, S. L., Jakosky, B. M., Matousek, S., & Edwards, C. (2020). *MARS ORBITERS FOR SURFACE, ATMOSPHERE AND IONOSPHERE CONNECTIONS (MOSAIC).* 2.

Lillis, R., Luhmann, J. G., Ma, Y., Barjatya, A., Brain, D., Thiemann, E., Modolo, R., Harada, Y., Larson, D., Curry, S., Whittlesey, P., Livi, R., Hara, T., Curtis, D., Taylor, E., & Parker, J. (2022). *ESCAPADE: Mars' first smallsat science mission will unveil its unique hybrid magnetosphere*. *44*, 420.

Mack, C. A. (2013). Generating random rough edges, surfaces, and volumes. *Applied Optics*, *52*(7), 1472. https://doi.org/10.1364/AO.52.001472

Marouf, E. A., & Tyler, G. L. (1982). Microwave Edge Diffraction by Features in Saturn's Rings: Observations with Voyager 1. *Science*, *217*(4556), 243–245. https://doi.org/10.1126/science.217.4556.243

McCleese, D. J., Schofield, J. T., Taylor, F. W., Calcutt, S. B., Foote, M. C., Kass, D. M., Leovy, C. B., Paige, D. A., Read, P. L., & Zurek, R. W. (2007). Mars Climate Sounder: An investigation of thermal and water vapor structure, dust and condensate distributions in the atmosphere, and energy balance of the polar regions. *Journal of Geophysical Research*, *112*(E5), E05S06. https://doi.org/10.1029/2006JE002790

Miyamoto, M., Imamura, T., Tokumaru, M., Ando, H., Isobe, H., Asai, A., Shiota, D., Toda, T., Häusler, B., Pätzold, M., Nabatov, A., & Nakamura, M. (2014). RADIAL DISTRIBUTION OF COMPRESSIVE WAVES IN THE SOLAR CORONA REVEALED BY *AKATSUKI* RADIO OCCULTATION OBSERVATIONS. *The Astrophysical Journal*, *797*(1), 51. https://doi.org/10.1088/0004-637X/797/1/51

Moeller, G., Ao, C. O., & Mannucci, A. J. (2020). *A cubesat mission concept for the remote sensing of the Martian atmosphere* [Preprint]. Atmospheric Sciences. https://doi.org/10.1002/essoar.10504459.1

Nava, B., Kashcheyev, A., Migoya-Orue, Y., Radicella, S. M., Parrott, J., Sánchez-Cano, B., Witasse, O., Svedhem, H., Titov, D., & Ao, C. O. (2020). *Mutual radio occultation experiment between ExoMars Trace Gas Orbiter and Mars Express: Feasibility study and preparation for the data analysis*. EPSC2020-299.

Oudrhiri, K., Yang, O., Buccino, D., Kahan, D., Withers, P., Tortora, P., Matousek, S., Lay, N., Lazio, J., Krajewski, J., & Klesh, A. (2020). MarCO Radio Occultation: How the First Interplanetary Cubesat Can Help Improve Future Missions. *2020 IEEE Aerospace Conference*, 1–10. https://doi.org/10.1109/AERO47225.2020.9172734

Renno, N. O., & Kok, J. F. (2007). *Electrical activity and dust lifting on Earth, Mars, and beyond*.

Renno, N. O., Wong, A.-S., Atreya, S. K., de Pater, I., & Roos-Serote, M. (2003). Electrical discharges and broadband radio emission by Martian dust devils and dust storms: MARTIAN DUST DEVILS AND DUST STORMS. *Geophysical Research Letters*, *30*(22). https://doi.org/10.1029/2003GL017879

Roberts, J. H., Lillis, R. J., & Manga, M. (2009). Giant impacts on early Mars and the cessation of the Martian dynamo. *Journal of Geophysical Research*, *114*(E4), E04009. https://doi.org/10.1029/2008JE003287

Ruf, C., Renno, N. O., Kok, J. F., Bandelier, E., Sander, M. J., Gross, S., Skjerve, L., & Cantor, B. (2009). Emission of non-thermal microwave radiation by a Martian dust storm. *Geophysical Research Letters*, *36*(13), L13202. https://doi.org/10.1029/2009GL038715

Rummel, J., Stabekis, P., Devincenzi, D., & Barengoltz, J. (2002). COSPAR's planetary protection policy: A consolidated draft. *Advances in Space Research*, *30*(6), 1567–1571.

Scheeres, D., McMahon, J., Bierhaus, E. B., Wood, J., Benner, L., Hartzell, C., Hayne, P., Hopkins, J., Jedicke, R., Le Corre, L., Naidu, S., Pravec, P., & Ravine, M. (2020). *Janus: A NASA SIMPLEx mission to explore two NEO Binary Asteroids* [Other]. oral. https://doi.org/10.5194/epsc2020-930

Schoolcraft, J., Klesh, A. T., & Werne, T. (2016, May 16). MarCO: Interplanetary Mission Development On a CubeSat Scale. *SpaceOps 2016 Conference*. SpaceOps 2016 Conference, Daejeon, Korea. https://doi.org/10.2514/6.2016-2491

Smith, M. D., Wolff, M. J., Lemmon, M. T., Spanovich, N., Banfield, D., Budney, C. J., Clancy, R. T., Ghosh, A., Landis, G. A., Smith, P., Whitney, B., Christensen, P. R., & Squyres, S. W. (2004). First Atmospheric Science Results from the Mars Exploration Rovers Mini-TES. *Science*, *306*(5702), 1750–1753. https://doi.org/10.1126/science.1104257

Streeter, P. M., Lewis, S. R., Patel, M. R., Holmes, J. A., & Kass, D. M. (2020). Surface Warming During the 2018/Mars Year 34 Global Dust Storm. *Geophysical Research Letters*, *47*(9). https://doi.org/10.1029/2019GL083936

Sweeney, D., Ao, C., Vergados, P., Renno, N., Kass, D., & Martinez, G. (2021). Enabling Mars Radio Occultation by Smallsats. *2021 IEEE Aerospace Conference (50100)*, 1–12. https://doi.org/10.1109/AERO50100.2021.9438147

Sydnor, R. L. (1993). *Annual Precise Time and Time Interval (PTTI) Applications and Planning Meeting (24th) Held in McLean, VA on December 1-3, 1992*. NATIONAL AERONAUTICS AND SPACE ADMINISTRATION GREENBELT MD GODDARD SPACE ….

Tamppari, L. K., Barnes, J., Bonfiglio, E., Cantor, B., Friedson, A. J., Ghosh, A., Grover, M. R., Kass, D., Martin, T. Z., Mellon, M., Michaels, T., Murphy, J., Rafkin, S. C. R., Smith, M.

D., Tsuyuki, G., Tyler, D., & Wolff, M. (n.d.). *Expected atmospheric environment for the Phoenix landing season and location*. 18.

Tellmann, S., Pätzold, M., Häusler, B., Hinson, D. P., & Tyler, G. L. (2013). The structure of Mars lower atmosphere from Mars Express Radio Science (MaRS) occultation measurements: MaRS ATMOSPHERIC MEASUREMENTS. *Journal of Geophysical Research: Planets*, *118*(2), 306–320. https://doi.org/10.1002/jgre.20058

Thomas, J. B. (1999). *An Analysis of Gravity-Field Estimation Based on Intersatellite Dual-1-Way Biased Ranging*. 195.

Thorsos, E. I. (1988). The validity of the Kirchhoff approximation for rough surface scattering using a Gaussian roughness spectrum. *The Journal of the Acoustical Society of America*, *83*(1), 78–92. https://doi.org/10.1121/1.396188

Trainer, M. G., Wong, M. H., McConnochie, T. H., Franz, H. B., Atreya, S. K., Conrad, P. G., Lefèvre, F., Mahaffy, P. R., Malespin, C. A., Manning, H. L. K., Martín-Torres, J., Martínez, G. M., McKay, C. P., Navarro-González, R., Vicente-Retortillo, Á., Webster, C. R., & Zorzano, M. (2019). Seasonal Variations in Atmospheric Composition as Measured in Gale Crater, Mars. *Journal of Geophysical Research: Planets*, *124*(11), 3000–3024. https://doi.org/10.1029/2019JE006175

Tricomi, F. G. (1985). *Integral equations* (Vol. 5). Courier Corporation.

Vogt, M. F., Withers, P., Fallows, K., Flynn, C. L., Andrews, D. J., Duru, F., & Morgan, D. D. (2016). Electron densities in the ionosphere of Mars: A comparison of MARSIS and radio occultation measurements: ELECTRON DENSITIES AT MARS. *Journal of Geophysical Research: Space Physics*, *121*(10), 10,241-10,257. https://doi.org/10.1002/2016JA022987

Ware, R., Exner, M., Feng, D., Gorbunov, M., Hardy, K., Herman, B., Kuo, Y., Meehan, T., Melbourne, W., Rocken, C., Schreiner, W., Sokolovskiy, S., Solheim, F., Zou, X., Anthes, R., Businger, S., & Trenberth, K. (1996). GPS Sounding of the Atmosphere from Low Earth Orbit: Preliminary Results. *Bulletin of the American Meteorological Society*, *77*(1), 19–40. https://doi.org/10.1175/1520-0477(1996)077<0019:GSOTAF>2.0.CO;2

Werndl, C. (2016). On Defining Climate and Climate Change. *The British Journal for the Philosophy of Science*, *67*(2), 337–364. https://doi.org/10.1093/bjps/axu048

Wertz, J. R., Everett, D. F., & Puschell, J. J. (Eds.). (2011). *Space mission engineering: The new SMAD*. Microcosm Press : Sold and distributed worldwide by Microcosm Astronautics Books.

Williams, D. (2022, November 10). *Mars Fact Sheet*. Mars Fact Sheet. https://nssdc.gsfc.nasa.gov/planetary/factsheet/marsfact.html

Withers, P. (2009). A review of observed variability in the dayside ionosphere of Mars. *Advances in Space Research*, *44*(3), 277–307. https://doi.org/10.1016/j.asr.2009.04.027

Withers, P. (2010). Prediction of uncertainties in atmospheric properties measured by radio occultation experiments. *Advances in Space Research*, *46*(1), 58–73. https://doi.org/10.1016/j.asr.2010.03.004

Withers, P. (2012). Empirical Estimates of Martian Surface Pressure in Support of the Landing of Mars Science Laboratory. *Space Science Reviews*, *170*(1–4), 837–860. https://doi.org/10.1007/s11214-012-9876-2